纖維鋅礦結構氧化鎂鋅的高壓拉曼散射研究

研究生: 曾俊榮　　指導教授:周武清 教授

國立交通大學電子物理研究所

中文摘要

本研究利用拉曼頻譜技術來探討鎂原子和外加壓力對氧化鎂鋅(鎂含量介於 0 與 10 莫耳百分比) 之晶格動力學及晶體特性所造成的影響。由於摻雜鎂原子和施以外加壓力對氧化鋅聲子振動行為的改變明顯不同，因此可用來定義具有爭議性的 202.7，332.7 和 511.5 cm^{-1} 聲子振動模。精細的高壓拉曼實驗結果顯示氧化鎂鋅金屬化的相轉變壓力會隨著鎂濃度增加而下降，這個實驗結果是因為鎂導致晶體的離子性和非等向性增加所造成。實驗可測量得到的橫向有效電荷(單原子些微移動所造成的單位位移電偶矩)可用來探討氧化鎂鋅的晶體離子性。此外，我們也分析縱向和橫向光學聲子模的 E_1-A_1 聲子分裂，由拉曼技術觀察到的 E_1-A_1 聲子分裂情形可以進一步了解氧化鎂鋅的晶體非等向性隨壓力的關係。

Raman scattering study of wurtzite $Zn_{1-x}Mg_xO$ under high pressure

Student: Chun-Jung Tseng Advisor: Prof. Wu-Ching Chou

Institute of Electrophysics

National Chiao Tung University

Abstract

This study explores the effects of both Mg and pressure on the lattice dynamics and crystalline properties in $Zn_{1-x}Mg_xO$ ($0 \leqq x \leqq 0.10$) using Raman spectroscopy. The incorporation of Mg and the application of external pressure cause distinct phonon vibrational behaviors in ZnO. Accordingly, the 202.7, 332.7, and 511.5 cm^{-1} phonons, which were controversially assigned, can be defined. Detailed high-pressure Raman results show that the pressure-induced metallic phase transition pressure of $Zn_{1-x}Mg_xO$ decreases with incresing Mg content. This fact is a consequence of Mg-induced increase in both crystal ionicity and anisotropy. The experimentally measureable transverse effective charge, which is defined as a dipole moment per unit displacement induced by slight movement of an atom, is adopted to trace the crystal ionicity of $Zn_{1-x}Mg_xO$. Additionally, the E_1-A_1 splitting of the longitudinal and transverse optical phonon modes is analyzed which yields insight into the pressure-dependent crystal anisotropy of $Zn_{1-x}Mg_xO$ via Raman techniques.

Acknowledgement

幾經波折的碩班歷程不知不覺中也到了尾聲了，四年的時間當中，其中兩年因教書的關係而暫時離開實驗室，真的很感謝周老師及彥丞學長願意繼續帶領我完成學業，這些日子來，我從一張白紙逐漸有了色彩，從一個研究上的門外漢慢慢地開始瞭解研究的技巧和樂趣，從實驗室中我學到了很多有趣的知識和經驗，而這些是我在外面學不到的，這些經驗將讓我受用無窮。

首先，我要感謝我的指導老師周武清教授，提供我這麼豐富的資源，並且給予我寶貴的意見，讓我在研究上能夠很順利，另外，還要感謝李明知老師，徐子民老師，沈志霖老師，謝振豪老師，能夠在百忙之中擔任我的口試委員，並且給予我許多寶貴的指導，另外，也要再次感謝謝振豪老師提供這套實驗的樣品，讓我能夠有不錯的研究成果，同時，我要特別感謝彥丞學長這些日子來的指導，從實驗、分析、論文、投影片，每個環節都有學長的指導，才能讓我的研究如此的豐富精彩，在每次的討論中，都能感受到學長的研究精神，學長總是對自我的要求很高，每個小細節都很注意，實在是令人佩服。

接下來還要感謝實驗室的學長們，感謝李寧學長、文忠學長、瑞泰學長、崑峯學長，感謝學長們在研究上提供寶貴的經驗給我，另外，感謝學弟妹們的陪伴與幫忙，希望大家都能順利完成學業，進入理想的公司，另外，還要感謝畢業的鏡學、復凱、威智，感謝你們之前的幫忙與支持。

最後，我要感謝我的家人，讓你們為我擔心了，尤其是要感謝太太，沒能在坐月子的時候照顧妳及女兒，讓妳辛苦了，今後我會把所有時間都給你們，最後，把完成這份論文的喜悅獻與所有幫忙過我的人分享。

Contents

Chapter 1 Introduction

An urgent and worldwide need for renewable energy sources has aroused widespread research interest into potential photovoltaic materials; such research efforts may pave the way to gradual phase out nuclear power. Oxides are one of the promising materials owing to their natural availability, environmental stability, and eco-friendly characteristics [1]. Moreover, due to its large electronegativity, oxygen forms chemical bonds with almost all elements to give the corresponding oxides. Zinc oxide (ZnO) is a wide bandgap (~ 3.4 eV at 300 K) semiconductor and crystallizes preferentially in the hexagonal wurtzite type structure. Compared to ZnSe and GaN, the relatively strong polar binding, deep excitonic level (~ 60 meV), and biocompatibility with organic systems make ZnO highly attractive for functional optoelectronic devices [2~10]. Upon substitution of an increasing fraction of the Zn atoms by Mg, the band gap of $Zn_{1-x}Mg_xO$ can be engineered toward deep ultraviolet region [11,12]. Additionally, the ionic radius of Mg^{2+} (0.57 Å) closely matches to that of Zn^{2+} (0.60 Å), making this ternary alloy suitable for a barrier material in ZnO-based heterostructures [2,4~6,11] and solar-blind devices [12].

The technological importance has been motivating detailed and fundamental investigations of $Zn_{1-x}Mg_xO$ as well as their application-oriented researches. Although the optical properties of $Zn_{1-x}Mg_xO$ have been extensively studied, the effects of both Mg and

pressure on the lattice dynamics and crystalline stability of $Zn_{1-x}Mg_xO$ remain unexplored, in particular the transverse effective charge, crystal anisotropy, phase transitions, and phonon deformation potentials. Previous Raman studies on ZnO at ambient and high pressure conditions obtained partly unclear and contradictory results. (i) The origins of the vibrational modes at 202.7, 332.7, and the phonon at 511.5 cm^{-1} which appears only after intentional doping are controversially discussed [14~18]. (ii) The signs of the pressure-dependent LO-TO splitting and transverse effective charge in ZnO are contrary. Decremps *et al.* and Manjón *et al.* found that the LO-TO splitting and the transverse effective charge of the E_1 mode in ZnO increase upon compression [19,20]. However, Reparaz *et al.* demonstrated a decreasing behavior for both A_1 and E_1 modes with increasing pressure [21]. (iii) Previous high-pressure Raman measurements show that the wurtzite-to-rocksalt phase transition of ZnO completes at around 8.3 - 9.0 GPa [19,20,22]. The values are far below the experimental result (above 12.8 GPa) made from high resolution angular dispersive x-ray diffraction (XRD)[23]. Such a deviation is likely due to weak signal intensity, large pressure interval, and undetected low-frequency (< 100 cm^{-1}) E_2 vibrational phonon. Therefore, these evident inconsistencies are also strong motivations for a thorough study on the high-pressure Raman phonon dynamics in $Zn_{1-x}Mg_xO$.

In this paper, Raman scattering of $Zn_{1-x}Mg_xO$ ($0 \leqq x \leqq 0.10$) are studied systematically as a function of Mg composition at ambient condition and under hydrostatic

pressure. In order to investigate thoroughly the lattice dynamics and crystalline stability of the $Zn_{1-x}Mg_xO$, both the upstroke and downstroke high-pressure Raman measurements are carefully performed. The origins of the vibrational modes at 202.7, 332.7, and 511.5 cm^{-1} are determined based on the high-pressure Raman results. Additionally, the pressure dependence of the transverse effective charge, the crystal anisotropy, and the pressure-induced metallic phase transition of $Zn_{1-x}Mg_xO$ with various Mg concentrations are also studied.

This thesis is organized as follows. This chapter introduces the fundamental properties of $Zn_{1-x}Mg_xO$ semiconductors. Chapter 2 introduces the high-pressure and micro-Raman techniques used in this thesis. Chapter 3 discusses the effects of both Mg and pressure on the lattice dynamics and crystalline properties in $Zn_{1-x}Mg_xO$. Finally, Chapter 4 summarizes this thesis.

References

[1] D. E. Scaife, Sol. Energy **25**, 41 (1980).

[2] A. Tsukazaki, A. Ohtomo, T. Kita, Y. Ohno, and M. Kawasaki, Science **315**, 1388 (2007).

[3] H. T. Yuan, H. Shimotani, A. Tsukazaki, A. Ohtomo, M. Kawasaki, and Y. Iwasa, Adv. Funct. Mater. **19**, 1046 (2009).

[4] A. Tsukazaki, S. Akasaka, K. Nakahara, Y. Ohno, H. Ohno, D. Maryenko, A. Ohtomo, and M. Kawasaki, Nature Mater. **9**, 889 (2010).

[5] M. Nakano, A. Tsukazaki, K. Ueno, R. Y. Gunji, A. Ohtomo, T. Fukumura, and M. Kawasaki, Appl. Phys. Lett. **96**, 052116 (2010).

[6] K. Nakahara, S. Akasaka, H. Yuji, K. Tamura, T. Fujii, Y. Nishimoto, D. Takamizu, A. Sasaki, T. Tanabe, H. Takasu, H. Amaike, T. Onuma, S. F. Chichibu, A. Tsukazaki, A. Ohtomo, and M. Kawasaki, Appl. Phys. Lett. **97**, 013501 (2010).

[7] E. Y. M. Teraoka, D. H. Broaddus, T. Kita, A. Tsukazaki, M. Kawasaki, A. L. Gaeta, and H. Yamada, Appl. Phys. Lett. **97**, 071105 (2010).

[8] G. Adamopoulos, A. Bashir, W. P. Gillin, S. Georgakopoulos, M. Shkunov, M. A. Baklar, N. Stingelin, D. D. C. Bradley, and T. D. Anthopoulos, Adv. Funct. Mater. **21**, 525 (2011).

[9] H. J. Bolink, E. Coronado, D. Repetto, and M. Sessolo, Appl. Phys. Lett. **91**, 223501 (2007).

[10] M. Sessolo and H. J. Bolink, Adv. Mater. **23**, 1829 (2011).

[11] A. Ohtomo, M. Kawasaki, T. Koida, K. Masubuchi, H. Koinuma, Y. Sakurai, Y. Yoshida, T. Yasuda, and Y. Segawa, Appl. Phys. Lett. **72**, 2466 (1998).

[12] Q. Zheng, F. Huang, K. Ding, J. Huang, D. Chen, Z. Zhan, and Z. Lin, Appl. Phys. Lett. **98**, 221112 (2011).

[13] T. Makino, Y. Furuta, Y. Segawa, A. Tsukazaki, A. Ohtomo, Y. Hirayama, R. Shen, S. Takeyama, Y. Takagi, and M. Kawasaki, Phys. Rev. B **80**, 155333 (2009).

[14] J. M. Calleja and M. Cardona, Phys. Rev. B **16**, 3753 (1977).

[15] R. Cuscó, E. Alarcón-Lladó, J. Ibáñez, L. Artús, J. Jiménez, B. Wang, M. J. Callahan, Phys. Rev. B **75**, 165202 (2007).

[16] A. Kaschner, U. Haboeck, Martin Strassburg, Matthias Strassburg, G. Kaczmarczyk, A. Hoffmann, C. Thomsen, A. Zeuner, H. R. Alves, D. M. Hofmann, and B. K. Meyer, Appl. Phys. Lett. **80**, 1909 (2002).

[17] C. Bundesmann, N. Ashkenov, M. Schubert, D. Spemann, T. Butz, E. M. Kaidashev, M. Lorenz, and M. Grundmann, Appl. Phys. Lett. **83**, 1974 (2003).

[18] F. J. Manjón, B. Marí, J. Serrano, and A. H. Romero, J. Appl. Phys. **97**, 053516 (2005).

[19] F. Decremps, J. Pellicer-Porres, A. M. Saitta, J. C. Chervin, and A. Polian, Phys. Rev. B **65**, 092101 (2002).

[20] F. J. Manjón, K. Syassen, and R. Lauck, High Press. Res. **22**, 299 (2002).

[21] J. S. Reparaz, L. R. Muniz, M. R. Wagner, A. R. Goñi, M. I. Alonso, A. Hoffmann, and B. K. Meyer, Appl. Phys. Lett. **96**, 231906 (2010).

[22] S. J. Chen, Y. C. Liu, C. L. Shao, C. S. Xu, Y. X. Liu, L. Wang, B. B. Liu, and G. T. Zou, J. Appl. Phys. **99**, 066102 (2006).

[23] H. Liu, Y. Ding, M. Somayazulu, J. Qian, J. Shu, D. Häusermann, and H. K. Mao, Phys. Rev. B **71**, 212103 (2005).

Chapter 2
Experiments

In this chapter, we will introduce the experimental setup and techniques that were used in our study. The experimental setup includes Diamond Anvil Cell and micro-Raman system.

2.1 High-pressure Technique

2.1.1 Diamond Anvil Cell

The high pressure environment is generated by diamond anvil cell(DAC). The schematic illustration of the DAC, which is a convenient tool for optical measurements, is shown in Fig. 2-1. The principle of all high-pressure cells can be described as follows. A force ***F*** is applied to a small surface area(S), creating a pressure ***P = F/S.*** One can produce ultra-high pressure by reducing the size of the surface area (culet) of diamonds. The DAC is a convenient and easy tool to operate. The sample which is placed between two brilliant-cut diamonds is put into a thin metallic foil (gasket). As the applied force pushes the two opposite anvils together, the two opposite diamond anvils are compressed to each other, producing high pressure environment. The culets are separated by a thin gasket, which was predrilled with a circular hole (sample chamber) by using an electrical discharge machine. The culets of the diamonds are all 500 μm. The thickness of the gasket is about 0.3~0.2 mm. The sample chamber is around 170μm in diameter. After the sample is loaded into sample room, a drop of pressure-transmitting medium is filled to ensure hydrostatic conditions.

In the Fig.2-1, “A” is the hemisphere rockers on which the diamond anvil was mounted; “B” is diamond; “C” is a gasket. A spring lever-arm is employed to generate force on the diamond surfaces. Force is applied through the lever-arm by turning the screws, which make

the two opposite diamonds pressing mutually. Therefore, a hydrostatic and continuous varying pressure conditions are obtained.

2.1.2 Pressure Medium

To obtain a hydrostatic pressure environment within the sample chamber, a pressure medium is required. Traditionally, water is considered as a bad pressure medium because it transfers to solid ice VI and VII at 0.6 and 2.1 GPa, respectively. The 4:1 methanol-ethanol mixed liquid as a pressure-transmitting medium, which is widely used in high-pressure measurements, is used in our experiments. The hydrostatic pressure was determined by the spectral shift of the ruby R1 line. The R1-R2 splitting in the ruby fluorescence was maintained well up to 25.4 Gpa as shown in Fig.2-2.

2.1.3 Pressure Calibration

Various methods of pressure calibration involving the DAC have been used. Pressure in the DAC was estimated by calculating force over area, the known fixed point and the internal makers such as NaCl or silver in high-pressure X-ray studies. These methods are not convenient and are often proved to be inaccurate.

In 1972, the calibration of pressure in the DAC was overcome and became the most convenient method later. This breakthrough was successful because of the use of visual microscopic studies in the DAC. Foreman *et al*. first calibrated the shift of the R-line ruby fluorescence peaks as a function of pressure in the DAC, and demonstrated that this shift could be used as a convenient internal pressure calibration [1]. The technique incorporates a ruby crystal with the sample of interest and measures the pressure dependence of the sharp ruby R1 line fluorescence. The R-line of Cr^{3+}–droped Al_2O_3 shifts linearly to long wavelength with hydrostatic pressure in the range of 0.1 ~ 22.0 GPa. The R-line broadens if the ruby experiences non-hydrostatic stresses. A tiny ruby chip of 5-10μm along with the sample in the pressure medium is excited by an Ar-ion laser. Figure 2-3 shows the energy levels and the resulting absorption and luminescence for Cr^{3+} ions in ruby [2].

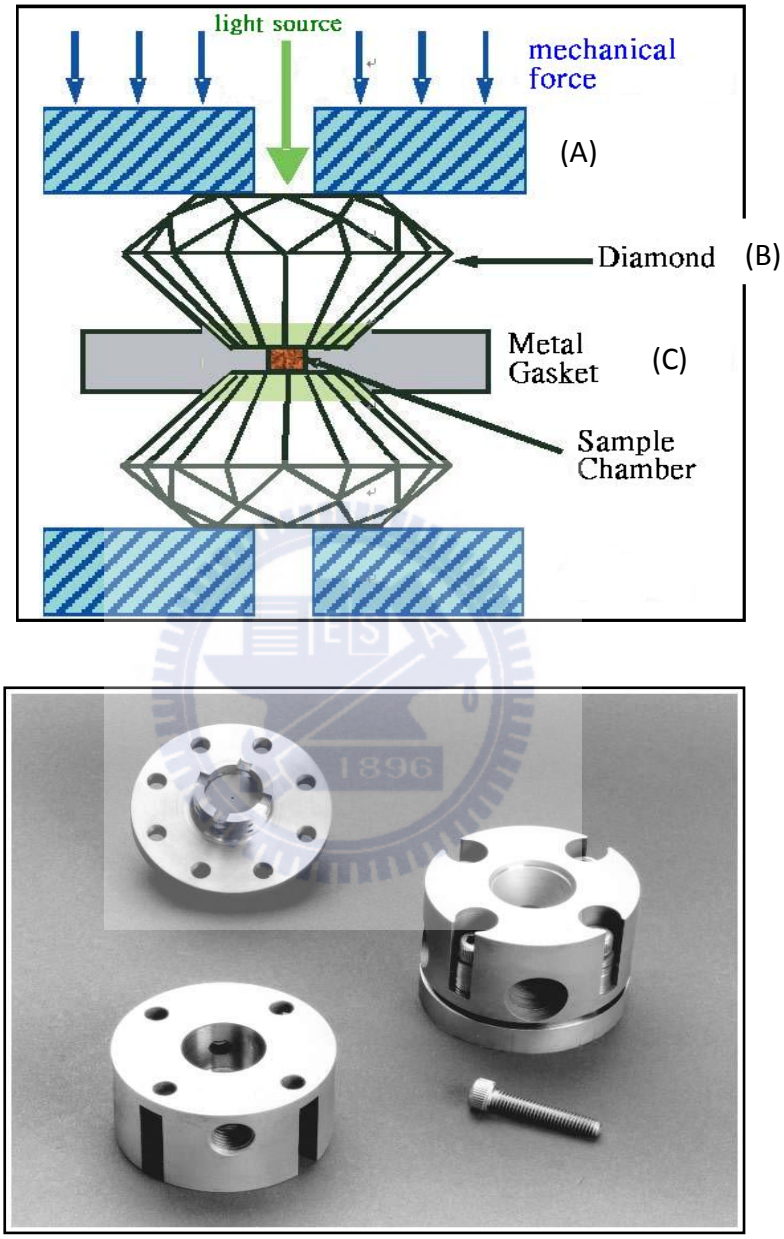

Fig.2-1 Basic setup of diamond anvil cell

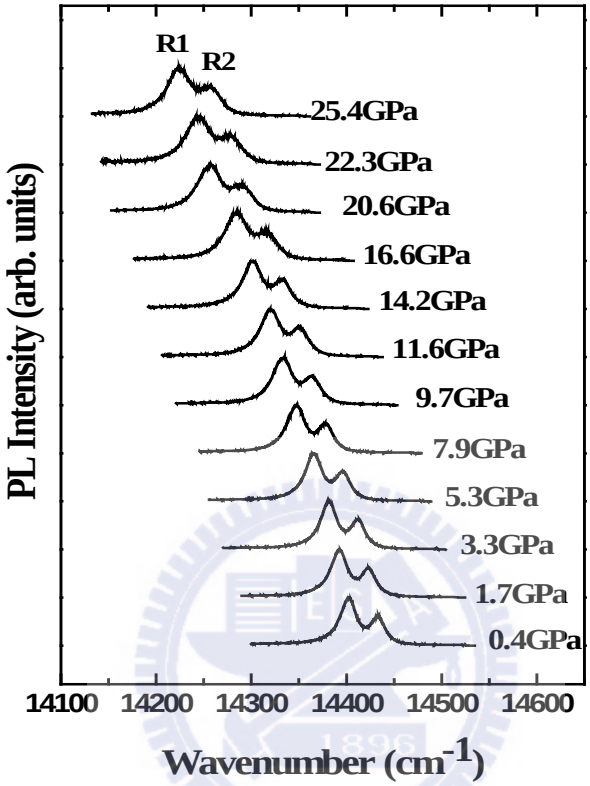

Fig.2-2 Ruby fluorescence obtained by obtained by using pressure medium of 4:1 methanol-ethanol mixed liquid verse applied pressure. The righ-hand and left-hand side peaks of the plots present R1 and R2 peaks of the ruby fluorescence lines, respectively.

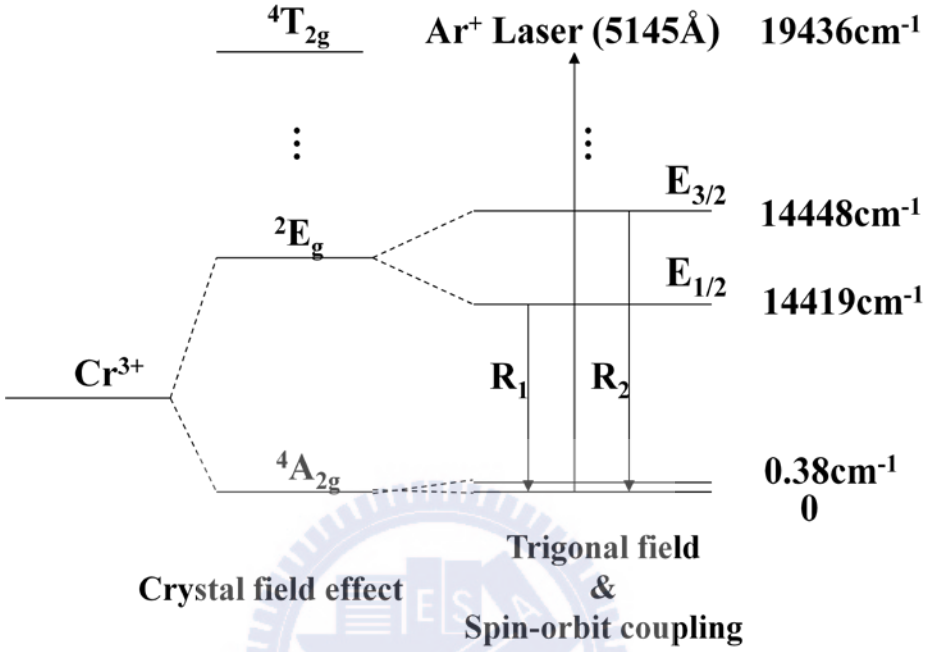

Fig.2-3 Energy level of Cr^{3+}. The transitions of $E_{1/2}$ to A and $E_{3/2}$ to A give rise to R1 And R2 lines, respectively.

2.2 Micro-Raman Scattering Experiments

2.2.1 The Principle of Raman Scattering

In 1928, C. V. Raman, Indian physicist, first observed the inelastic scattering phenomenon of light in materials. When light encounters the surface of a semiconductor, most part of the light will be elastically scattered (Rayleigh scattering). There is no change in photon frequency during these elastic interactions. However, a small fraction of the light interact inelastically with phonon modes, producing outgoing photons whose frequencies are shifted from the incoming ones. This interaction of incident light with optical phonons called Raman scattering. When the polarization of optical phonon is transverse (longitudinal) relative to their wavevector of photon, it is call TO (LO) mode. The photon loses energy by emitting a phonon (Stokes shifted) or gains energy by absorbing a phonon (anti-Stokes shifted). The law of conservation energy and momentum must be applied in the process. The conservation conditions can be written as

$$h\nu_s = h\nu_i \pm h\nu_0 \quad (2.1)$$

$$k_s = k_i \pm k_0 \quad (2.2)$$

Where ν_i and ν_s are the incoming and scattered photon frequencies, respectively, k_i and k_s are the incoming and scattered photon wavevector, respectively, while ν_0 and k_0 are the phonon frequency and wavevector, respectively. The intensity of the anti-Stokes modes is normally much weaker than that of the Stokes modes. Raman scattering is inherently a weak process, but lasers provide enough power such that the spectra can be routinely measured [3].

All the Raman parameters – frequency and intensity, line shape and linewidth, polarization behavior – can be used to characterize the lattice, impurities, and free carriers in a semiconductor. The intensity gives information about the crystalline conditions. The linewidths increase when a material is damaged or disordered, because these conditions

increase the phonon damping or break the momentum conservation during the Raman scattering process. The frequencies of the phonons can be used to determine the degree of alloying in a ternary material [4].

2.2.2 Experimental Setup

In Fig. 2-4, the schematic diagram of the Raman scattering experiment is shown. In this work, the Raman scattering measurements were performed by a Jobin-Yvon micro-Raman system. The Raman spectra were collected in backscattering configuration and at room temperature by using the 514.5 nm line of an Ar^{+}-ion laser as excitation. The intensity of Raman lines were normalized to the laser power as measured by a power meter. Usually, a laser beam with a power of 90 mW was focused to a size of ~5μm on the sample surface in the DAC. To exclude the Reyleigh scattering, the 514.5 nm holographic notch plus filter was used to filter out the Reyleigh scattering of the laser. The spectra were analyzed by a iHR550 spectrometer equipped with a multichannel LN_2-cooled charge-coupled device (CCD). Finally, the spectrometer was contraolled by a computer, which was used to store and plot the collected data.

2.2.3 Experimental Process

$Zn_{1-x}Mg_xO$ powders were synthesized by the citric acid assisted sol-gel method in an aqueous solution using stoichiometric zinc nitrate hexahydrate [$Zn(NO_3)_2 \cdot 6H_2O$] and magnesium nitrate hexahydrate [$Mg(NO_3)_2 \cdot 6H_2O$]. The mixture was first heated and stirred in 80 ^oC water bath until the formation of gels, followed by further heating up to 120 ^oC in a furnace for 12 h to evaporate the solvent. Finally, the powders were post-annealed at 800 ^oC in air for 2 h to remove the organic residuals. To obtain high pressure up to about 20GPa, the $Zn_{1-x}Mg_xO$ powders and ruby chip (about 1μm in size) were sealed with the pressure transmitting medium in the sample chamber which was a hole of 170μm in diameter and 100μm thick drilled on gasket which has an original thickness of 250μm. The $Zn_{1-x}Mg_xO$ powders were loaded along with ruby chip into a diamond anvil cell. The pressure determination was done by reading the peak position of the ruby R1 fluorescence line. The pressure gradient was less than 0.5 GPa, as determined by measurements made at various positions of the sample chamber.

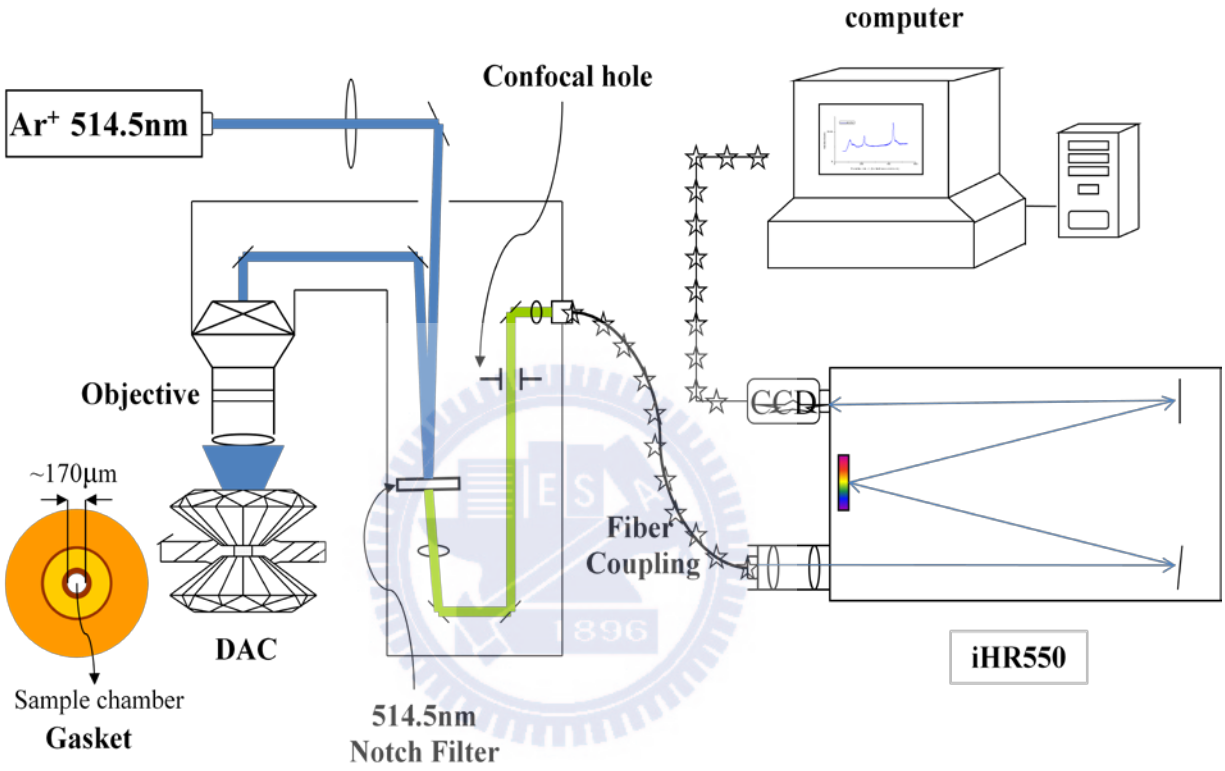

Fig. 2-4 Schematic diagram of micro-Raman system

References

[1] R.A.Forman, G.J.Piermarini, J.D.Barnett, and S.Block, Science **176**, 284 (1972)

[2] E.Huang, J. Geol. Soc. China **32**, 924(1992)

[3] I.F.Chang and S.S.Mitra, Phys. Rev **172**, 924(1968)

[4] A.Chergui, J.Valenta, and J.L.Loison, Semiconductor Science Technology **9**, 2073 (1994).

Chapter 3 Results and Discussion

In this chapter, Raman scattering of $Zn_{1-x}Mg_xO$ ($0 \leqq x \leqq 0.10$) are studied systematically as a function of Mg composition at ambient condition (Sec. 3.1) and under hydrostatic pressure (Sec. 3.2). In order to investigate thoroughly the lattice dynamics and crystalline stability of the $Zn_{1-x}Mg_xO$, both the upstroke and downstroke high-pressure Raman measurements are carefully performed.

3.1 Raman scattering study of $Zn_{1-x}Mg_xO$ at ambient pressure

Fig. 3-1 shows the SEM images of the $Zn_{1-x}Mg_xO$ (x = 0 and 10 %) powders. The average crystalline sizes(d_{size}) for ZnO and ZnMgO powders are about 300 and 500 *nm* in diameter, respectively. A slight increase in particle size can be observed as Mg is incorporated. The $Zn_{1-x}Mg_xO$ particle sizes ($a_B << d_{size} \approx \lambda_{exc}$) are far above the ZnO exciton Bohr radius (a_B ~ 2.34 *nm*) [1] and close to the excitation wavelength (λ_{exc}), which means the quantum confinement and the size effects can be neglected. Figure 3-2 shows clear Raman spectra of $Zn_{1-x}Mg_xO$ (x = 0, 3, 7, and 10 %) at 300 K and ambient condition together with mode assignments for the observed peaks. According to the group theory at the Γ point of the Brillouin zone, the optical phonons in ZnO wurtzite structure belong to the irreducible representations: $\Gamma_{opt} = A_1 + E_1 + 2E_2 + 2B_1$, where the A_1 and E_1 phonons are both Raman and

IR active, the E_2 phonons are only Raman active, and the B_1 phonons are silent. As shown in Fig.3-3, both E_1 and E_2 phonons are associated with the atomic motions in *a*-*b* plane whereas the atomic motions of A_1 and B_1 phonons take place along the *c* axis.The crystal anisotropy induces splitting of the A_1 and E_1 phonons; these polar modes further split into longitudinal optical (LO) and transversal optical (TO) components due to the long-range Coulomb interaction. The symmetry of nonpolar E_2 phonons are denoted as E_2^{low} and E_2^{high}, representing the lower and higher frequency branch due to the vibrations of heavier and lighter atoms, respectively. Totally, there are six Raman-active optical phonon modes in ZnO wurtzite structure. Compared to the well-defined orientation of the *c* axes for bulks and films on specific substrates, the crystal-axes of powders are randomly tilted relative to the laser excitation polarization. Therefore, the peculiar crystalline geometries, along with the large angular aperture of the focusing objective (N.A. = 0.35) result in the observation of all Raman phonon modes.

As can be seen in Fig. 3-2, for undoped ZnO sample, the two intense peaks of E_2^{low} (98.8 cm^{-1}) and E_2^{high} (438.3 cm^{-1}) dominate the entire Raman spectrum. The phonon peaks appear at 380.6 and 411.1 cm^{-1} are assigned to the A_1(TO) and E_1(TO) phonons, respectively. A broad and asymmetric phonon at around 580.0 cm^{-1} comprises two adjacent peaks of A_1(LO) and E_1(LO) phonons at 574.4 and 584.0 cm^{-1}, respectively. In addition to the above mentioned phonons, three modes at 202.7, 332.7 cm^{-1}, and 511.5 cm^{-1} (x > 0) are also found. The origins

of these phonons are still controversial and will be discussed later. All the observed Raman phonon frequencies and the comparisons with previous works for ZnO are reported in Table 3-1. In this work, the zone-center optical phonons are observable at both Stokes and anti-Stokes sides of each Raman spectrum. Moreover, the phonon frequencies are all identical under various excitations (457.9, 488.0, and 514.5 *nm*).

In order to get a deeper insight on the lattice dynamics of $Zn_{1-x}Mg_xO$ ($0 \leqq x \leqq 0.10$), the highlighted zone-center optical phonons are displayed in Fig.3-4(a)(c). The phonon frequency and the LO-TO splitting for each phonon are listed in Table 3-2. Clearly, as Mg is substituted into ZnO, the A_1, E_1, and E_2^{low} [Fig.3-4(b)] phonons together with the acoustic phonons shift toward higher frequencies. However, the E_2^{high} [Fig.3-4(c)] and 332.7 cm^{-1} phonons behave oppositely. These phonon shifts are accompanied by intensity quenching and linewidth broadening, which could be attributed to Mg-induced translational crystal asymmetry and alloy fluctuations. Additionally, as shown in Table 3-2, the LO-TO splittings for both A_1 and E_1 modes increase with increasing Mg content. The results imply that ZnO becomes more *ionic* when Mg is incorporated. This behavior correlates well with the fact that the ionicity (f_i; Phillips' ionic scale) of MgO (0.841) is larger than that of ZnO (0.616) [3].

In general, the substitution of Mg for Zn atoms declines the reduced mass of the oscillator, as a result, the Raman phonons shift toward higher frequencies. However, it is not the case for the E_2^{high} and 332.7 cm^{-1} phonons. This is because the E_2^{high} phonon corresponds

mainly (~ 85 %) [4] to the vibrations of the oxygen (lighter) atoms, thus, the influence of Mg on the E_2^{high} phonon is nearly negligible. The difference in atomic masses, $m_{Mg}(24) < m_{Zn}(65)$, cannot be the reason for the decreasing of E_2^{high} phonon frequency. As previously demonstrated, the lattice constant a of $Zn_{1-x}Mg_xO$ increases monotonically with x [5]. Therefore, it is the lattice expansion in a-b plane accounting for the E_2^{high} phonon softening (see Fig.3-3). This result indicates that the E_2^{high} phonon vibration is more sensitive to the lattice constant than the cation mass. Similar trend is also found for the vibrational mode at 332.7 cm^{-1} previously assigned to either the transverse acoustic overtone at K-M-Σ point [6] or the difference between the E_2^{high} and E_2^{low} in ZnO [2]. As x is increased, the phonon frequency correlates well with the difference between E_2^{high} and E_2^{low} modes. Moreover, the phonon shift agrees well with the opposite vibrational behaviors of E_2^{low} and E_2^{high} phonons. These experimental results reveal that the $E_2^{high} - E_2^{low}$ complex phonon is highly likely the origin of the 332.7 cm^{-1} mode. Such an assignment will be further confirmed under high pressure measurements.

In addition to the host Raman phonons of ZnO, a vibrational mode at 511.5 cm^{-1}(denotes as D hereafter) is observed when Mg is intentionally incorporated. Interestingly, with increasing Mg content the intensity of D mode slightly enhances but its frequency remains unchanged. The origin of this phonon was controversially discussed. Kaschner *et al.* reported the observation of this additional phonon in N-doped ZnO films and interpreted the

occurrence as N-related local vibrational mode due to N in substitutional O site [7]. However, Bundesmann *et al.* disputed this interpretation since they detected the phonon in ZnO films doped with Fe, Sb, and Al, intentionally grown without N incorporation [8]. Due to the large differences in mass among these dopants, the authors suggested the intrinsic host lattice defects as the origin. Manjón *et al.* attributed this phonon in N-doped ZnO films to the disorder-activated 2 B_1^{low} mode due to the relaxation of Raman selection rules induced by the breakdown of the crystal symmetry [9].

In the present case, the *D* mode cannot be ascribed to N-related phonon because the $Zn_{1-x}Mg_xO$ powders are all grown without additional N-doping and it is invisible in ZnO. Also, the *D* mode cannot be an activated silent B_1^{low} mode because:(i) the silent modes are both Raman and IR forbidden, (ii)B_1-related phonons have not been observed in $Zn_{1-x}Mg_xO$ even under high-pressure conditions (higher crystal asymmetry), and (iii) the *D* mode behaves entirely different from B_1^{low} which should shift toward higher frequencies with increasing *x* (see Fig.3-3). Based on these observations, a structure or a complex defect with different crystal symmetry to the host lattice is accounted for the *D* mode in $Zn_{1-x}Mg_xO$ ($x > 0$). Therefore, in our study we suggest the complex defects of Zn and O interstitials (Zn_I-O_I) induced by Mg incorporation as its origin. Zinc (oxygen) vacancies and antisites can be ruled out since they degrade the entire crystal isotropy without providing related phonon modes [10]. Further evidences for the Zn_I-O_I complexes will be discussed later under high pressure.

3.2 Raman scattering study of $Zn_{1-x}Mg_xO$ under high pressure

Fig. 3-5(a) shows the pressure-dependent Raman spectra of ZnO recorded with increasing pressure up to 20.0 GPa. The pressure dependence of the phonon frequencies are illustrated in Fig. 3-5(b), in which the frequency evolution can be fitted linearly (see Table 3-3). As the external pressure is applied, the reduction in lattice constants should shift all Raman phonons toward higher frequencies. However, two remarkable exceptions of the E_2^{low} and the 202.7 cm^{-1}(marked with an asterisk) phonons are found in Fig. 3-5(a).The softening of the E_2^{low} phonons on increasing pressure are observed in all the $Zn_{1-x}Mg_xO$ ($0 \leqq x \leqq 0.10$) samples discussed herein. Similar experimental result was also found in wurtzite GaN (see Table 3-4) [11]. As suggested by Saitta and Decremps, the soft C_{66} elastic constant is responsible for the negative pressure coefficient of the E_2^{low} phonon in GaN, InN, and ZnO [12]. However, it is not the case for wurtzite AlN, SiC, and BeO, which exhibit positive pressure coefficients in accordance with the calculated pressure dependence of the C_{66} elastic constant [12,13]. Previous assignments to the vibrational mode at 202.7 cm^{-1} are $2E_2^{low}$ or 2TA in terms of Raman measurements made at ambient pressure [2,6]. In the present study, we find that its frequency correlates well with that of the E_2^{low} phonon. Furthermore, the phonon shifts equally with the E_2^{low} phonon toward higher frequencies (as Mg content increases) or lower frequencies (as external pressure increases). Based on these facts, we can conclude that the 202.7 cm^{-1} phonon should have significant contribution of the E_2^{low} phonon,

thus, it can be assigned to 2 E_2^{low} mode.

As shown in Fig. 3-5(a), the pressure-induced phonon shifts are accompanied by significant fall in their intensities. With increasing pressure up to 9.6 GPa, the Raman spectra drastically change. Three additional phonons with similar intensities simultaneously appear at around 150, 550, and 590 cm^{-1}, respectively, and the latter two peaks overlap as a broad vibrational band in the range between 500 and 650 cm^{-1}. Above 9.6 GPa, the A_1(TO), A_1(LO), E_1(TO), and E_1(LO) phonons gradually vanish, and the Raman spectra are dominated by the 150, 550, and 590 cm^{-1} phonons. As the pressure further increases to 13.2 GPa, the two intense E_2^{low} and E_2^{high} phonons in wurtzite structure absolutely disappear, and the sample darkens. These phenomena are strong evidences of pressure-induced metallic phase transition [14~18]. In fact, the first-order Raman phonon modes are forbidden by the selection rules in rocksalt structures. Thus, the metallic phase transition should be accompanied by the wurtzite-to-rocksalt phase change as previously reported [19,20,21]. The wurtzite-to-rocksalt phase transition of ZnO finishes at around 13.2 GPa, determined using detailed high-pressure Raman measurements, agrees well with the previous high resolution angular dispersive XRD result (above 12.8 GPa) by Mao's group [22]. A close inspection of the three additional modes in Fig. 3-5(a) indicates that these phonons emerge at around 9.6 GPa and become pronounced with increasing pressure until the wurtzite-to-rocksalt phase transition finishes (~ 13.2 GPa). Clearly, these phonons are less sensitive to pressure than the first-order Raman phonons in the

wurtzite phase. In rocksalt phase, these additional phonons are still observable and slightly shift to higher frequencies with increasing pressure. The broad vibrational band within 500 to 650 cm^{-1} was also found in previous Raman spectra of ZnO at high pressure conditions [19,20]. Based on these findings, we can conclude that these additional Raman phonons appeared at high pressures are vibrational modes of rocksalt ZnO. The complicated Raman signals in the pressure range between 9.6 and 13.2 GPa reflect the coexistence of wurtzite and rocksalt phase, *i.e.*the ZnO undergoes a gradual phase transformation from wurtzite to rocksalt in accordance with the XRD results [22].

Fig. 3-6 and 3-7 show the upstroke pressure-dependent Raman spectra together with phonon frequencies of $Zn_{0.97}Mg_{0.03}O$ and $Zn_{0.93}Mg_{0.07}O$, respectively. Figure 3-8(a) and 8(b) show the upstroke pressure-dependent Raman spectra and phonon frequencies of $Zn_{0.90}Mg_{0.10}O$, respectively. As compared with ZnO, several interesting conclusions can be drawn. (i) In addition to the A_1, E_1, and E_2 phonons, the D mode whose frequency is not affected by the Mg concentration at ambient pressure shifts to higher frequencies with increasing pressure. (ii) The additional modes of $Zn_{0.90}Mg_{0.10}O$ appear at around 8.1 GPa. This result indicates that the onset of the wurtzite-to-rocksalt phase transition for $Zn_{0.90}Mg_{0.10}O$ is lower than that of ZnO (~ 9.6 GPa). (iii) The first-order Raman phonon modes in wurtzite phase including the intense E_2^{low} and E_2^{high} modes vanish at 10.4 GPa. Also, the color of the sample in the DAC suddenly changes from bright (at ambient pressure)

to dark (at 10.4 GPa) as shown in Fig. 3-9(a) and (b), respectively. In other words, the metallic phase transition of the $Zn_{0.90}Mg_{0.10}O$ finishes at around 10.4 GPa which value is lower than that of ZnO (~ 13.2 GPa).

Prior to discussing the effect of Mg on the phase transitions, we turn to studying the downstroke pressure-dependent Raman spectra of ZnO and $Zn_{0.90}Mg_{0.10}O$ as shown in Fig. 3-10(a) and 10(b), respectively. The downstroke pressure-dependent Raman spectra of $Zn_{0.97}Mg_{0.03}O$ and $Zn_{0.93}Mg_{0.07}O$ are shown in Fig. 3-11(a) and 3-11(b), respectively. Obviously, upon decompression the rocksalt phase is maintained beyond the upstroke phase-transition pressure for all the samples, showing substantial phase hysteresis. The ZnO and $Zn_{0.90}Mg_{0.10}O$ revert to the wurtzite phase, where the E_2^{low} and E_2^{high} phonons reappear first, at about 2.4 and 1.2 GPa, respectively. It is worth mention that the degree of phase hysteresis (pressure difference between the finish of the upward transition and the onset of downward transition) falls with increasing Mg content. Further releasing the pressure, the rest of the wurtzite-phase phonons including the *D* mode appear. Once the applied pressure is absolutely released, the samples exhibit a time independent behavior even after two months. Such an unusual hysteresis effect(> 10 GPa) was also found for AlN, GaN, InN, and zincblende (3*C*-type) SiC[23,24]. However, materials such as ZnSe, CdSe, and CdTe, exhibit quite small phase hysteresis (< 3 GPa). This is because the lattice compressibility is considerably higher for ZnSe(bulk modulus B_0 = 62.4 GPa), CdSe(B_0 = 53.1 GPa), and

CdTe(B_0 = 42.4 GPa)(considered to be softer because of their lower modulus values) than 3*C*-SiC (B_0 = 321.9 GPa), AlN (B_0 = 208.0 GPa), GaN (B_0 = 200.0 GPa), InN (B_0 = 125.5 GPa), and ZnO (B_0 = 135.3 GPa) [11,16,25~28]. The obtained upstroke and downstroke phase transition pressures for all the $Zn_{1-x}Mg_xO$ ($0 \leqq x \leqq 0.10$) are summarized in Table 3-3. Clearly, all the phase transition pressures decline with increasing Mg concentration. Due to the differences in atomic radius, mass, and electronegativity between Zn and Mg, the crystal becomes destabilized as the substituted Mg content increases. Moreover, the existence of Mg in ZnO may cause crystal defects (the *D* mode) which would soften the lattice by generating large distortions and increase the crystal anisotropy. These facts indicate that the substituted Mg atoms tend to reduce the crystalline stability and induce crystal defects, as a result, the phase transition pressures decline. Similar phenomena have been observed in other II-VI ternary compounds, such as ZnFeSe [14], ZnSeTe [15],ZnCdSe [16], ZnSe:Cl [17], and ZnMnTe [18].

Table 3-3 lists the linear pressure coefficients($d\omega_i/dp$) and the mode Grüneisen parameters (γ_i) of the zone-center optical phonons for all the $Zn_{1-x}Mg_xO$ samples. The mode Grüneisen parameter is defined using the relation [29],

$$\gamma_i = -\left(\frac{d\ln\omega_i}{d\ln V}\right) = \left(\frac{B_0}{\omega_{i0}}\right)\left(\frac{d\omega_i}{dp}\right), \quad (1)$$

where ω_i denotes the phonon mode frequency, ω_{i0} indicates the phonon frequency at ambient pressure, B_0 is the bulk modulus defined as the inverse of the isothermal compressibility, and

V is the molar volume in cm^3/mol. In the present work, B_0 = 135.3 GPa obtained from high-resolution XRD approach is adopted for all the samples [25]. As shown in Table 3-3, several conclusions can be summarized. (i) The phonon pressure coefficients, $d\omega_i/dp$ and γ_i, for E_2^{low} phonons are all negative values. Moreover, the pressure coefficients of $d\omega_i/dp$ for the $E_2^{high} - E_2^{low}$ mode are in excellent agreement with the subtracted values between individual E_2^{high} and E_2^{low} phonons. These peculiar pressure-dependent phonon behaviors are strong evidences further confirming its assignment. (ii) The $d\omega_i/dp$ and γ_i of the D mode remain nearly unchanged over the entire Mg range of interest($0.03 \leqq x \leqq 0.10$). Moreover, its phonon pressure coefficient $d\omega_i/dp$ is very close to the values of A_1(TO) and E_2^{high} phonons whose vibrations correspond mainly to the oxygen atoms. These experimental results reveal that the complex Zn_I-O_I defects with different crystal symmetry to the host lattice induced by additional element incorporation is highly likely the origin of the D mode.(iii) The trends, $d\omega_{LO}/dp < d\omega_{TO}/dp$ and $\gamma_{LO} < \gamma_{TO}$, are found through out the samples, indicating that the LO-TO splitting falls with increasing pressure.(iv) The pressure coefficients for the A_1 modes are all less than those for the E_1 modes irrespective of their transverse or longitudinal character, reflecting that the E_1-A_1 splitting increases with increasing pressure.

Fig. 3-12(a) and 3-12(b) show the pressure-dependent LO-TO splitting of $Zn_{1-x}Mg_xO$ ($0 \leqq x \leqq 0.10$) for A_1 and E_1 modes, respectively. In both cases, it is clear that the LO-TO splitting diminishes under pressure. Table 3-4 compares the phonon pressure coefficients of

ZnO with III-V compounds AlN, GaN, and InN. Obviously, the trend, $d\omega_{TO}/dp < d\omega_{LO}/dp$, is found for all these III-V materials, while ZnO is the only material exhibits a pressure-induced decrease of the LO-TO splitting. This result agrees well with observations made for other II-VI compounds such as ZnSe and ZnTe [14,18], where the LO-TO splitting decreases with pressure. However, as shown by the data in Fig 3-12 and Table 3-5, the sign of the $d(\Delta\omega)/dp$ and $\gamma_{\text{LO-TO}}$ for ZnO are in clear contrast with the previous study by Decremps and co-workers [19], implying a different pressure dependence of crystal ionicity in ZnO.

To study the crystal ionicity of $Zn_{1-x}Mg_xO$, the transverse or Born effective charge (e_T^*) was calculated using the relation (in SI units) [19],

$$(e_T^*)^2 = 4\pi^2 V \mu \varepsilon_0 \varepsilon_\infty (\omega_{LO}^2 - \omega_{TO}^2), \quad (2)$$

where V is the volume per pair, μ is the reduced mass of an anion-cation pair, ε_0 is the vacuum permittivity, ε_∞ is the high frequency dielectric constant, and ω_{LO} (ω_{TO}) is the experimental Raman phonon frequency. For the reduced mass of $Zn_{1-x}Mg_xO$ we use the equation: $\mu = \{M_O \times [xM_{Mg} + (1-x)M_{Zn}]\} / \{M_O + [xM_{Mg} + (1-x)M_{Zn}]\}$, where M_O, M_{Zn}, and M_{Mg} are the atomic weights of O, Zn, and Mg, respectively. The high-frequency dielectric constant of $Zn_{1-x}Mg_xO$ is taken as $\varepsilon_\infty(x) = (1-x)\varepsilon_\infty(\text{ZnO}) + x\varepsilon_\infty(\text{MgO})$, where the value ε_∞(ZnO) = $3.95\varepsilon_0$ and ε_∞(MgO) = $2.94\varepsilon_0$ at ambient pressure are used in this study[19,30,31].The calculated transverse effective charge values at ambient condition are reported in Table 3-5. The values are 2.10e and 2.01e(with e the elementary electron charge) for the ZnO A_1 and E_1

modes, respectively. These values correlate closely with previous studies [19,32]. Similar to the LO-TO splitting, a slight increase in e_T^* for both A_1 and E_1 modes is found as the Mg content is increased. This result is a consequence of an effective transfer of charge from the cation Zn to the anion O, which can be interpreted by saying that ZnO becomes more *ionic* upon the incorporation of Mg. The degree of ionicity is an important factor that determines the pressure-induced phase transition pressure. For example, the highly *covalent* material SiC starts to transform into rocksalt phase at ~ 100 GPa with the reverse transition begins at ~ 35 GPa. However, the less *covalent* GaN starts to transform at a much lower pressure of ~ 37 and 25 GPa for upward and downward transition, respectively [23]. The higher *ionic* materials such as MgO and CdO even favor rocksalt phase at ambient pressure.

The pressure-dependent transverse effective charge for $Zn_{1-x}Mg_xO$ ($0 \leqq x \leqq 0.10$) can be determined from the measured phonon frequencies using Eq. (2). The reduction of the unit-cell volume with hydrostatic pressure is described by the Murnaghan equation of state [33]. For the pressure-dependent ε_∞, we use $d\varepsilon_\infty/dp = -0.014\varepsilon_0$ GPa^{-1}[19]. The resulting transverse effective charge values are plotted as a function of pressure in Fig. 3-13(a) and 3-13(b) for A_1 and E_1 modes, respectively. For comparison, the e_T^* is normalized to its value at ambient pressure. The obtained parameters de_T^*/dp, $\gamma_{e_T^*}$, and $d[e_T^*/e_T^*(0)]/dp$ for all the samples are all negative values (see Table 3-5). Moreover, the experimental results for wurtzite AlN and GaN [11], and zincblende SiC and GaAs are also plotted for comparison in

Fig. 3-13 [27,34]. It is clear that the $e_T^* / e_T^*(0)$ falls under compression for all the $Zn_{1-x}Mg_xO$ samples, *i.e.* the $Zn_{1-x}Mg_xO$ becomes more *covalent* at high pressures. This experimental phenomenon is similar to GaAs and GaN (slight decrease), but is in clear contrast to that of SiC and AlN (see Fig.3-13 and Table 3-6). For ZnO, the decreasing behavior again contrasts with the previous work by Decremps *et al.* who found an increased pressure-dependent $e_T^* / e_T^*(0)$ [19]. Interestingly, we found that the effects of Mg and external pressure on the transverse effective charge of ZnO are contrary. At ambient pressure, ZnO becomes more *ionic* upon the incorporation of Mg, while it becomes more *covalent* upon compression. Consequently, the substituted Mg atoms tend to reduce the pressure dependence of the LO-TO splitting and the transverse effective charge in $Zn_{1-x}Mg_xO$.

For a wurtzite structure, the crystal anisotropy,$\Delta(c/a)$, is determined by the deviation of the c/a ratio from its ideal value (1.633), *i.e.* $\Delta(c/a) = c/a - 1.633$[33]. It has been pointed out that the phonon frequency ratio $[\omega_{E_1(TO)} - \omega_{A_1(TO)}] / \omega_{E_1(TO)}$ is proportional to the structural anisotropy of a given structure[34]. Thus, there might be relations between the phonon frequency ratio $[\omega_{E_1(TO)} - \omega_{A_1(TO)}] / \omega_{E_1(TO)}$ measured by high-pressure Raman scattering and the crystal anisotropy $\Delta(c/a)$ obtained from high-pressure XRD measurements for $Zn_{1-x}Mg_xO$. Fig. 3-14 shows the dependence of $[\omega_{E_1(TO)} - \omega_{A_1(TO)}] / \omega_{E_1(TO)}$ on $\Delta(c/a)$ and pressure for $Zn_{0.90}Mg_{0.10}O$ with c/a = 1.602 and $d(c/a)/dp$ = -0.0005 GPa^{-1} [35,37]. Significantly, in both cases a linear relationship is found and the evolution can be described using the following

fits,

$$[\omega_{E_1(TO)} - \omega_{A_1(TO)}] / \omega_{E_1(TO)} = s \cdot \Delta(c/a) = t \cdot P(GPa), \quad (3)$$

yielding the slope s = 1.59 and t = 7.92 × 10^{-4} cm^{-1}/GPa. The TO and LO phonon frequency ratios at ambient pressure along with the fitted slopes for all the samples are listed in Table 3-7. The TO (LO) phonon frequency ratio at ambient pressure is 0.048 (0.007), 0.061 (0.012), 0.074 (0.016), and 0.091 (0.021) for GaN [11], InN [36], ZnO, and AlN [11], respectively. These values qualitatively agree with the variation in $\Delta(c/a)$ for the above materials at ambient condition[35]. The results unambiguously show that the crystal anisotropy in ZnO is larger than that in GaN and InN but smaller than that in AlN. Based on the overall phonon frequency ratios and the fitted slopes shown in Table 3-7, we can conclude that both Mg and pressure increase the crystal anisotropy of ZnO. Accordingly, it is obvious that the higher Mg content in $Zn_{1-x}Mg_xO$, the faster the crystal becomes anisotropy, which results are in accordance with the Mg-induced decreasing of the phase transition pressures.

References

[1] R. T. Senger and K. K. Bajaj, Phys. Rev. B **68**, 045313 (2003).

[2] R. Cuscó, E. Alarcón-Lladó, J. Ibáñez, L. Artús, J. Jiménez, B. Wang, M. J. Callahan, Phys. Rev. B **75**, 165202 (2007).

[3] J. C. Phillips, Rev. Mod. Phys. **42**, 317 (1970).

[4] J. Serrano, F. J. Manjón, A. H. Romero, F.Widulle, R. Lauck, and M. Cardona, Phys. Rev. Lett. **90**, 055510 (2003).

[5] Y. Kim, K. Page, and R. Seshadri, Appl. Phys. Lett. **90**, 101904 (2007).

[6] J. M. Calleja and M. Cardona, Phys. Rev. B **16**, 3753 (1977).

[7] A. Kaschner, U. Haboeck, Martin Strassburg, Matthias Strassburg, G. Kaczmarczyk, A. Hoffmann, C. Thomsen, A. Zeuner, H. R. Alves, D. M. Hofmann, and B. K. Meyer, Appl. Phys. Lett. **80**, 1909 (2002).

[8] C. Bundesmann, N. Ashkenov, M. Schubert, D. Spemann, T. Butz, E. M. Kaidashev, M. Lorenz, and M. Grundmann, Appl. Phys. Lett. **83**, 1974 (2003).

[9] F. J. Manjón, B. Marí, J. Serrano, and A. H. Romero, J. Appl. Phys. **97**, 053516 (2005).

[10] A. Janotti and C. G. Van de Walle, Phys. Rev. B **76**, 165202 (2007).

[11] A. R. Goñi, H. Siegle, K. Syassen, C. Thomsen, and J.-M. Wagner, Phys. Rev. B **64**, 035205 (2001).

[12] A. M. Saitta and F. Decremps, Phys. Rev. B **70**, 035214 (2004).

[13] A. P. Jephcoat, R. J. Hemley, H. K. Mao, R. E. Cohen, and M. J. Mehl, Phys. Rev. B **37**, 4727 (1988).

[14] C. M. Lin, D. S. Chuu, T. J. Yang, W. C. Chou, J. Xu, and E. Huang, Phys. Rev. B **55**, 13641 (1997).

[15] C. S. Yang, W. C. Chou, D. M. Chen, C. S. Ro, J. L. Shen, and T. R. Yang, Phys. Rev. B **59**, 8128 (1999).

[16] Y. C. Lin, C. H. Chiu, W. C. Fan, S. L. Yang, D. S. Chuu, and W. C. Chou, J. Appl. Phys. **101**, 073507 (2007).

[17] Y. C. Lin, C. H. Chiu, W. C. Fan, C. H. Chia, S. L. Yang, D. S. Chuu, M. C. Lee, W. K. Chen, W. H. Chang, and W. C. Chou, J. Appl. Phys. **102**, 123510 (2007).

[18] Y. C. Lin, W. C. Fan, C. H. Chiu, F. K. Ke, S. L. Yang, D. S. Chuu, M. C. Lee, W. K. Chen, W. H. Chang, W. C. Chou, J. S. Hsu, and J. L. Shen, J. Appl. Phys. **104**, 013503 (2008).

[19] F. Decremps, J. Pellicer-Porres, A. M. Saitta, J. C. Chervin, and A. Polian, Phys. Rev. B **65**, 092101 (2002).

[20] F. J. Manjón, K. Syassen, and R. Lauck, High Press. Res. **22**, 299 (2002).

[21] S. J. Chen, Y. C. Liu, C. L. Shao, C. S. Xu, Y. X. Liu, L. Wang, B. B. Liu, and G. T. Zou, J. Appl. Phys. **99**, 066102 (2006).

[22] H. Liu, Y. Ding, M. Somayazulu, J. Qian, J. Shu, D. Häusermann, and H. K. Mao, Phys.

Rev. B **71**, 212103 (2005).

[23] A. Mujica, A. Rubio, A. Muñoz, and R. J. Needs, Rev. Mod. Phys. **75**, 863 (2003).

[24] C. Pinquier, F. Demangeot, J. Frandon,J.C. Chervin, A. Polian, B. Couzinet, P. Munsch,O. Briot, S. Ruffenach, B. Gil, and B. Maleyre, Phys. Rev. B **73**, 115211 (2006).

[25] H. Liu, Y. Ding, M. Somayazulu, J. Qian, J. Shu, D. Häusermann, and H. K. Mao, Phys. Rev. B **71**, 212103 (2005).

[26] C. Pinquier, F. Demangeot, J. Frandon,J.C. Chervin, A. Polian, B. Couzinet, P. Munsch,O. Briot, S. Ruffenach, B. Gil, and B. Maleyre, Phys. Rev. B **73**, 115211 (2006).

[27] D. Olego, M. Cardona, and P. Vogl, Phys. Rev. B **25**, 3878 (1982).

[28] S. Adachi, *Handbook on physical properties of semiconductors. Volume 3, II-VI Compound Semiconductors* (Springer - Verlag, 2004).

[29] M. Blackman and W. B. Daniels, in *Light Scattering in Solids IV*, edited by M. Cardona and G. Güntherodt (Springer, Berlin, 1984), Chap. 8.

[30] I. F. Chang and S. S. Mitra, Phys. Rev. **172**, 924 (1968).

[31] J. Chen and W. Z. Shen, Appl. Phys. Lett.**83**, 2154 (2003).

[32] J. S. Reparaz, L. R. Muniz, M. R. Wagner, A. R. Goñi, M. I. Alonso, A. Hoffmann, and B. K. Meyer, Appl. Phys. Lett. **96**, 231906 (2010).

[33] F. D. Murnaghan, Proc. Natl. Acad. Sci. U.S.A. **30**, 244 (1944).

[34] R. Trommer, H. Müller, M. Cardona, and P. Vogl, Phys. Rev. B **21**, 4869 (1980).

[35] P. Lawaetz, Phys. Rev. B **5**, 4039 (1972).

[36] K. Karch and F. Bechstedt, Phys. Rev. B **56**, 7404 (1997).

[37] S. Desgreniers, Phys. Rev. B **58**, 14102 (1998).

[38] V. Y. Davydov, V. V. Emtsev, I. N. Goncharuk, A. N. Smirnov, V. D. Petrikov, V. V. Mamutin, V. A. Vekshin, S. V. Ivanov,M. B. Smirnov, and T. Inushima, Appl. Phys. Lett. **75**, 3297 (1999).

[39] T. C. Damen, S. P. S. Porto, and B. Tell, Phys. Rev. **142**, 570 (1966).

Table 3-1. Room temperature Raman phonon frequencies and the comparisons with previous works for ZnO.

Phonon Mode (i)	Brillouin Zone Points/Lines	Phonon Frequency ω_i (cm^{-1})					
		This work	Ref. 6	Ref. 2	Ref. 19	Ref. 32	Ref. 39
E_2^{low}	Γ	98.8	101	99	99	98.1	101
$2E_2^{low}$; 2TA	Γ;*L*,*M*,*H*	202.7	208	203			
$E_2^{high} - E_2^{low}$; 2 Phonons	Γ;*K*-*M*-Σ	332.7	332	333			
A_1(TO)	Γ	380.6	380	378	382	377.4	380
E_1(TO)	Γ	411.1	408	410	414	410.9	407
E_2^{high}	Γ	438.3	437	438	439	437.9	437
2LA	*M*-*K*	485.0		483			
2LA	*L*,*M*,*H*	539.8	541	536			
A_1(LO)	Γ	574.4	574	574	574	577.9	574
E_1(LO)	Γ	584.0	584	590	580	587.2	583
TA+TO	*H*,*M*	615.8		618			
TA+LO	*L*,*H*	657.8		657			
TA+LO	*M*	666.2		666			
LA+TO	*M*	698.2		700			
LA+TO	*L*-*M*	720.5		723			

Table 3-2. Zone-center optical phonon frequencies and the LO-TO splittings for $Zn_{1-x}Mg_xO$ ($0 \leqq x \leqq 0.10$).

Phonon Mode	Phonon Frequency ω_i (cm^{-1})			
(i)	x = 0 %	x = 3 %	x = 7 %	x = 10 %
E_2^{low}	98.8	99.4	100.4	101.2
$E_2^{high} - E_2^{low}$	332.7	331.6	331.0	330.5
A_1(TO)	380.6	381.8	382.7	383.5
E_1(TO)	411.1	412.1	413.2	414.0
E_2^{high}	438.3	438.0	437.7	437.5
D	-	511.5	511.5	511.5
A_1(LO)	574.4	577.3	582.8	585.2
E_1(LO)	584.0	589.4	597.5	601.3
Phonon Splitting	Phonon Frequency $\Delta\omega$ (cm^{-1})			
A_1(LO) – A_1(TO)	193.8	195.5	200.1	201.7
E_1(LO) – E_1(TO)	172.9	177.3	184.3	187.3

Table 3-3. Linear pressure coefficients ($d\omega_i/dp$), mode Grüneisen parameters (γ_i), and phase transition pressures for $Zn_{1-x}Mg_xO$ ($0 \leqq x \leqq 0.10$).

Mg Content (x)	Phonon Mode (i)	$d\omega_i/dp$ (cm^{-1}/GPa)	Gruneisen Parameter (γ_i)	Phase Transition Pressure (GPa)
0%	E_2^{low}	-0.76	-1.04	
	$E_2^{high} - E_2^{low}$	5.67	2.31	
	A_1(TO)	4.73	1.68	9.6 ± 0.2^a
	E_1(TO)	4.98	1.64	13.2 ± 0.2^b
	E_2^{high}	4.86	1.50	2.6 ± 0.2^c
	A_1(LO)	4.14	0.98	
	E_1(LO)	4.32	1.00	
3%	E_2^{low}	-0.71	-0.97	
	$E_2^{high} - E_2^{low}$	5.52	2.25	
	A_1(TO)	4.67	1.65	9.2 ± 0.2^a
	E_1(TO)	4.95	1.63	12.6 ± 0.2^b
	E_2^{high}	4.77	1.47	2.4 ± 0.2^c
	D	4.61	1.22	
	A_1(LO)	4.26	1.00	
	E_1(LO)	4.49	1.03	
7%	E_2^{low}	-0.68	-0.92	
	$E_2^{high} - E_2^{low}$	5.41	2.21	
	A_1(TO)	4.62	1.63	8.5 ± 0.2^a
	E_1(TO)	4.97	1.63	11.8 ± 0.2^b
	E_2^{high}	4.70	1.45	1.8 ± 0.2^c
	D	4.64	1.23	
	A_1(LO)	4.32	1.00	
	E_1(LO)	4.60	1.04	
10%	E_2^{low}	-0.66	-0.88	
	$E_2^{high} - E_2^{low}$	5.33	2.18	
	A_1(TO)	4.60	1.62	8.1 ± 0.2^a
	E_1(TO)	4.96	1.62	10.4 ± 0.2^b
	E_2^{high}	4.62	1.43	1.4 ± 0.2^c
	D	4.62	1.22	
	A_1(LO)	4.38	1.01	
	E_1(LO)	4.71	1.06	

[a]The onset of wurtzite-to-rocksalt phase transition.

[b]The finish of wurtzite-to-rocksalt phase transition.

[c]The onset of rocksalt-to-wurtzite phase transition.

Table 3-4. Experimental pressure coefficients ($d\omega_i/dp$), the mode Grüneisen parameters (γ_i), and the LO-TO splittings in wurtzite ZnO, AlN, GaN, and InN.

	ZnO		AlN[a]		GaN[a]		InN[b]	
Mode	$d\omega_i/dp$ (cm^{-1}/GPa)	γ_i	$d\omega_i/dp$ (cm^{-1}/GPa)	γ_i	$d\omega_i/dp$ (cm^{-1}/GPa)	γ_i	$d\omega_i/dp$ (cm^{-1}/GPa)	γ_i
E_2^{low}	-0.76	-1.04	0.12	0.10	-0.30	-0.40	-	-
A_1(TO)	4.73	1.68	4.40	1.51	3.90	1.47	5.81	1.66
E_1(TO)	4.98	1.64	4.55	1.41	3.94	1.41	-	-
E_2^{high}	4.86	1.50	4.99	1.58	4.20	1.50	5.56	1.42
A_1(LO)	4.14	0.98	-	-	4.40	1.20	5.96	1.26
E_1(LO)	4.32	1.00	4.60	1.06	-	-	-	-
LO-TO Splitting	$\Delta\omega$ (cm^{-1})	$d(\Delta\omega)/dp$ (cm^{-1}/GPa)	$\Delta\omega$ (cm^{-1})	$d(\Delta\omega)/dp$ (cm^{-1}/GPa)	$\Delta\omega$ (cm^{-1})	$d(\Delta\omega)/dp$ (cm^{-1}/GPa)	$\Delta\omega$ (cm^{-1})	$d(\Delta\omega)/dp$ (cm^{-1}/GPa)
A_1	193.8	-0.60	-	-	205.3	0.40	152.2	0.15
E_1	172.9	-0.66	240.8	0.10	-	-	-	-

[a]Reference 11.

[b]Reference 38.

Table 3-5. Pressure coefficients of LO-TO splitting $\Delta\omega$ and transverse effective charge e_T^* (in units of the elementary charge e) for $Zn_{1-x}Mg_xO$ ($0 \leqq x \leqq 0.10$).

Mg (x)	LO-TO Splitting	$\Delta\omega$ (cm^{-1})	$d(\Delta\omega)/dp$ (cm^{-1}/GPa)	$\gamma_{\text{LO-TO}}$	e_T^* (e)	de_T^*/dp ($10^{-3}e$/GPa)	$\gamma_{e_T^*}$	$d[e_T^*/e_T^*(0)]/dp$ ($10^{-3}e$/GPa)
0%	A_1	193.8	-0.60	-0.42	2.10	-19.3	-1.24	-9.19
	A_1[a]	192.0	-	-	2.40	-	-	-
	A_1[b]	200.5	-0.36	-0.26	2.17	-14.6	-0.96	-6.70
	E_1	172.9	-0.66	-0.52	2.01	-14.9	-1.00	-7.40
	E_1[a]	166.0	0.93	0.80	2.02	6.4	0.45	3.02
	E_1[b]	176.3	-0.47	-0.38	2.04	-13.7	-0.96	-6.30
3%	A_1	195.5	-0.42	-0.29	2.11	-18.6	-1.19	-8.80
	E_1	177.3	-0.46	-0.35	2.05	-13.9	-0.92	-6.78
7%	A_1	200.1	-0.30	-0.20	2.13	-17.8	-1.13	-8.36
	E_1	184.3	-0.36	-0.26	2.09	-13.0	-0.84	-6.21
10%	A_1	201.7	-0.22	-0.15	2.15	-16.7	-1.05	-7.77
	E_1	187.3	-0.26	-0.19	2.11	-12.0	-0.77	-5.69

[a]Reference 19 (B_0 = 170.0 GPa).

[b]Reference 32 (B_0 = 142.6 GPa).

Table 3-6. Experimental pressure coefficients of transverse effective charge e_T^* in wurtzite ZnO, AlN, and GaN and zincblende SiC and GaAs.

Mode	ZnO		AlN[a]		GaN[a]		SiC[b]		GaAs[c]	
	$\frac{de_T^*}{dp}$	$\frac{d[e_T^*/e_T^*(0)]}{dp}$	$\frac{de_T^*}{dp}$	$\frac{d[e_T^*/e_T^*(0)]}{dp}$	$\frac{de_T^*}{dp}$	$\frac{d[e_T^*/e_T^*(0)]}{dp}$	$\frac{de_T^*}{dp}$	$\frac{d[e_T^*/e_T^*(0)]}{dp}$	$\frac{de_T^*}{dp}$	$\frac{d[e_T^*/e_T^*(0)]}{dp}$
	$(10^{-3}e/GPa)$		$(10^{-3}e/GPa)$		$(10^{-3}e/GPa)$		$(10^{-3}e/GPa)$		$(10^{-3}e/GPa)$	
A_1	-19.30	-9.19	-	-	-1.30	-0.48	4.92	1.83	-25.71	-11.79
E_1	-14.90	-7.40	0.15	0.06	-	-				

[a]Reference 11.

[b]Reference 28.

[c]Reference 29.

Table 3-7. Dependence of the TO and LO phonon frequency ratios on crystal anisotropy (in slope *s*) and pressure (in slope *t*) for $Zn_{1-x}Mg_xO$ ($0 \leqq x \leqq 0.10$).

	x = 0 %	x = 3 %	x = 7 %	x = 10 %
$[\omega_{E1(TO)} - \omega_{A1(TO)}] / \omega_{E1(TO)}$	0.074	0.074	0.074	0.074
slop *s*	1.30	1.37	1.47	1.59
slop *t* ($10^{-4}cm^{-1}$/GPa)	6.60	6.86	7.36	7.92
$[\omega_{E1(LO)} - \omega_{A1(LO)}] / \omega_{E1(LO)}$	0.016	0.021	0.025	0.027
slop *s*	0.65	0.66	0.75	0.76
slop *t* ($10^{-4}cm^{-1}$/GPa)	3.23	3.32	3.75	3.80

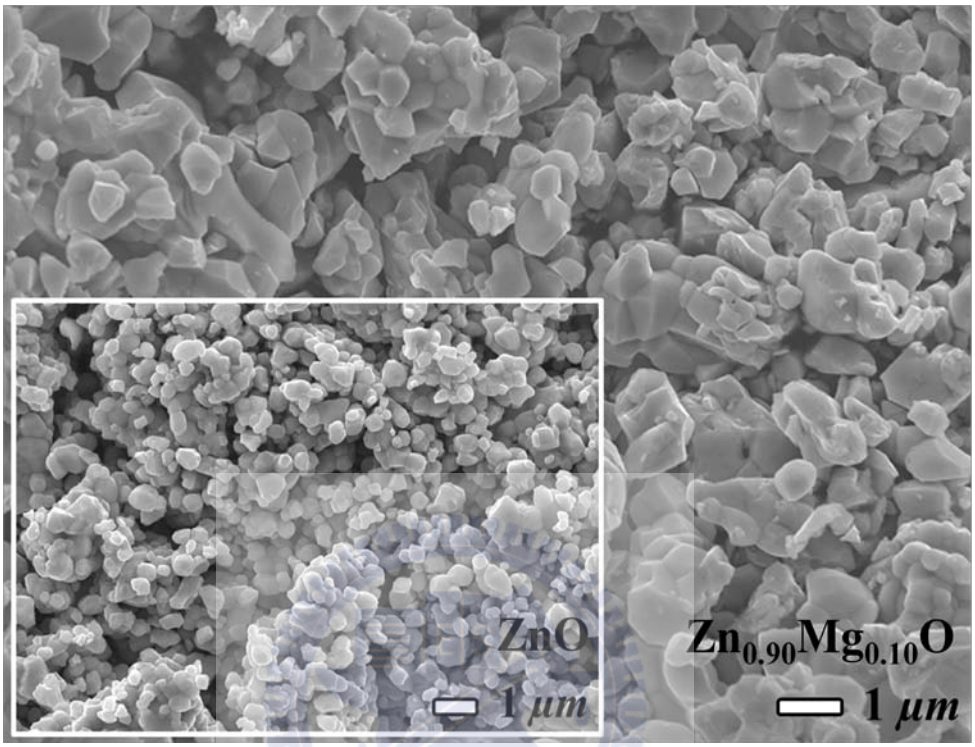

Fig.3-1 The SEM images of $Zn_{0.90}Mg_{0.10}O$ powders. The inset shows the pure ZnO powders.

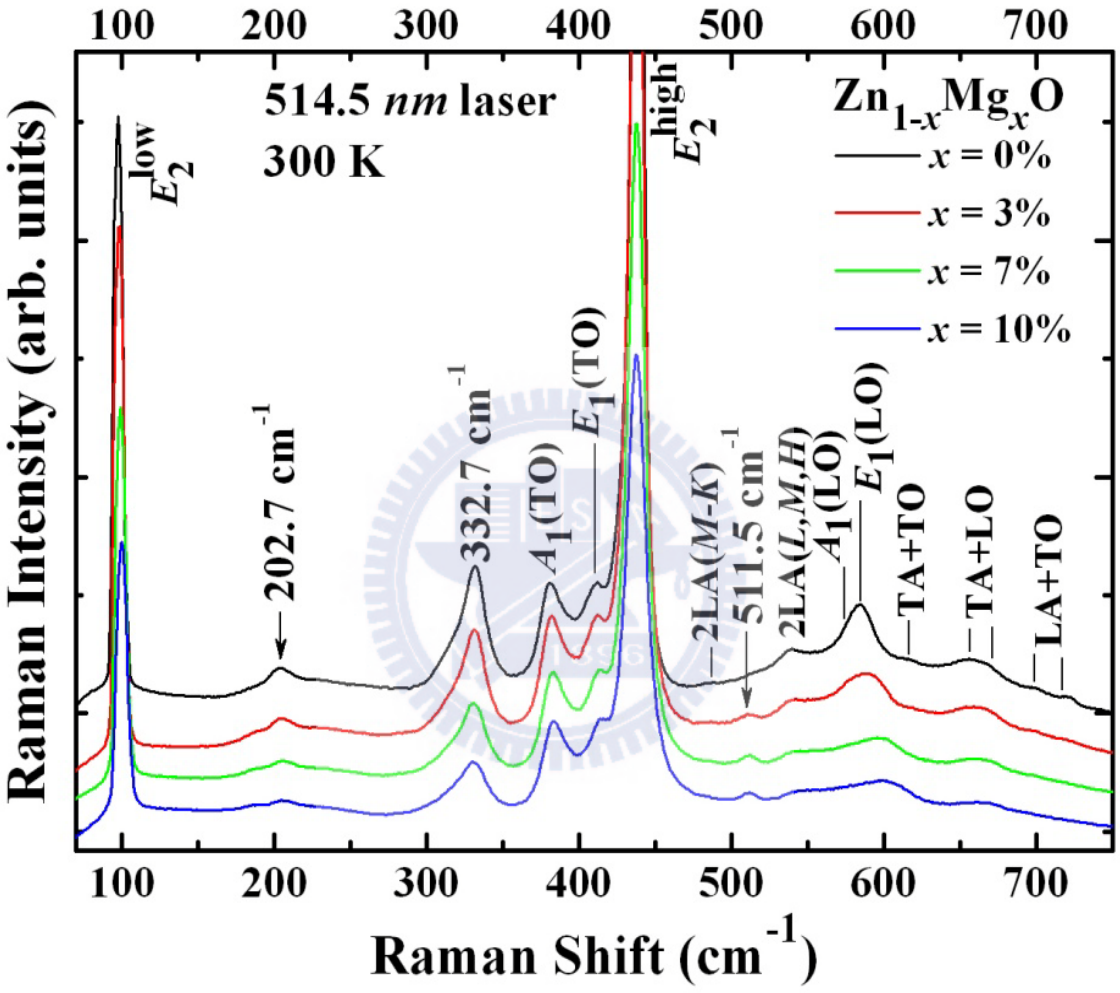

Fig.3-2 Raman spectra of $Zn_{1-x}Mg_xO$ (x = 0, 3, 7, and 10 %) at 300 K and under ambient pressure. The excitation source is a 514.5 *nm* line of an Ar^+ laser.

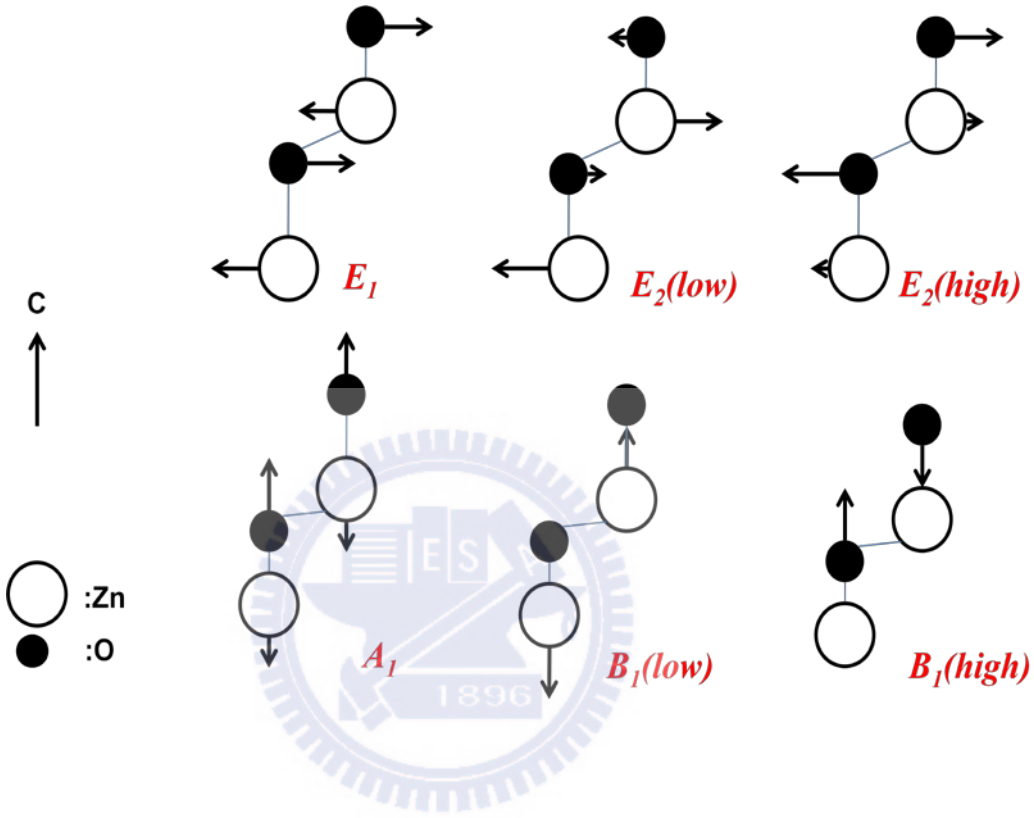

Fig. 3-3 Scheme of the displacement vectors for the six different optical phonon modes in wurtzite ZnO.

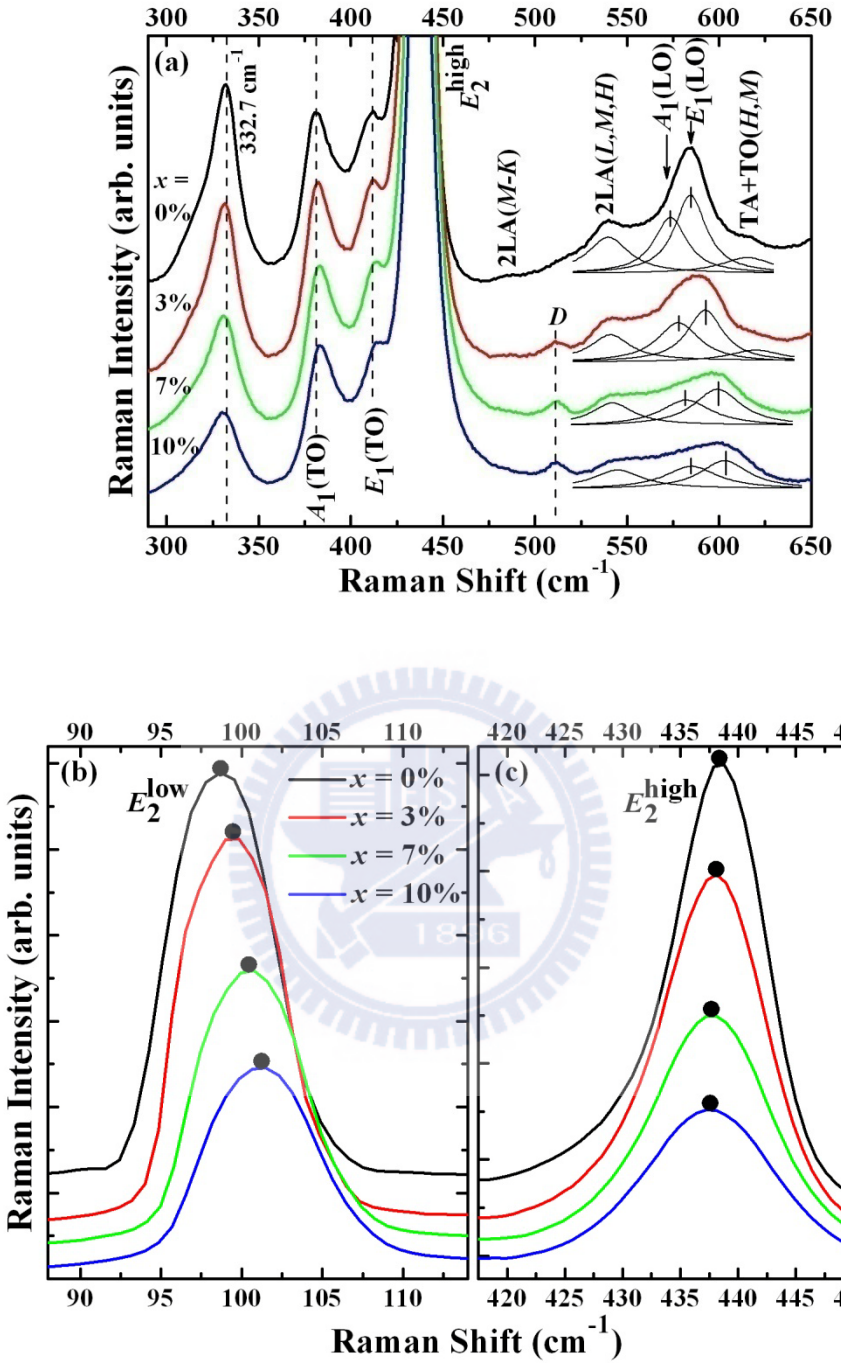

Fig.3-4 Highlighted zone-center Raman spectra for (a) A_1, E_1, D, and 332.7 cm^{-1} phonons, including Lorentzian fits for the LO modes, (b) E_2^{low}, and (c) E_2^{high} phonons of $Zn_{1-x}Mg_xO$ at 300 K and under ambient pressure. The dashed lines and solid circles are guides for the eyes.

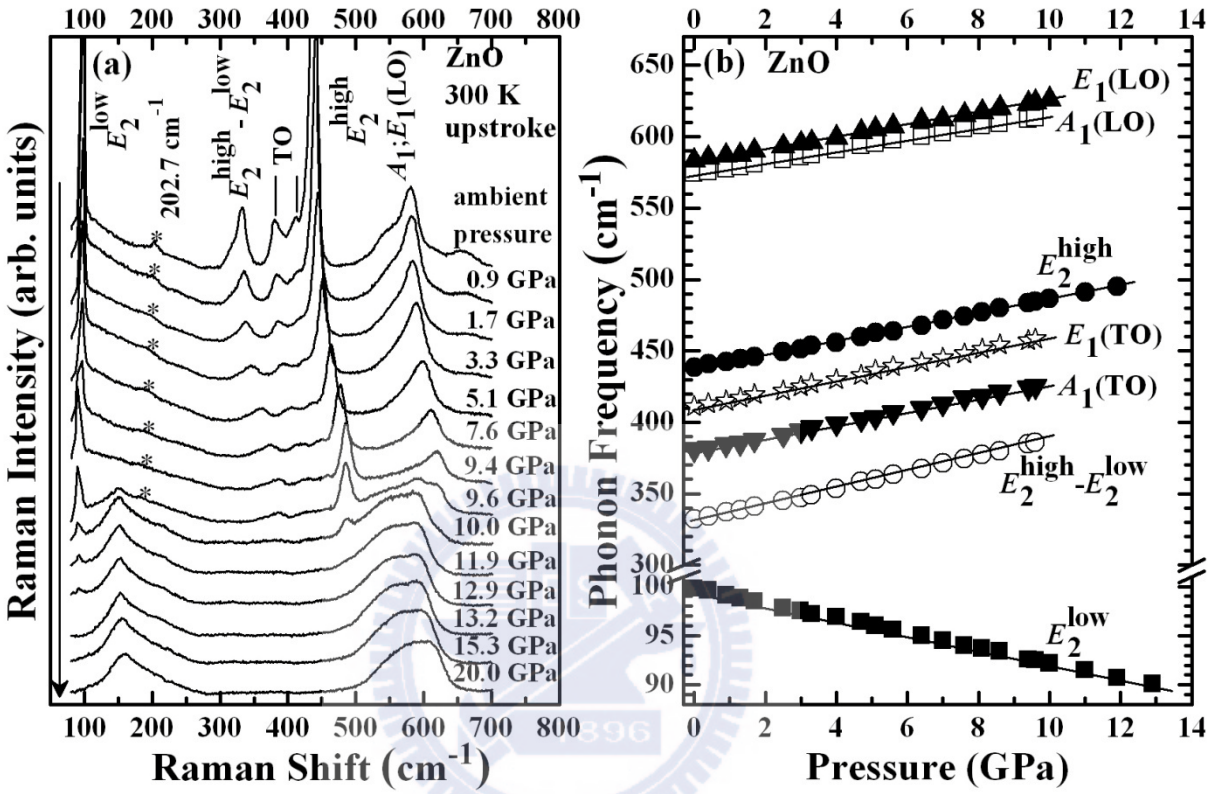

Fig. 3-5 (a) Upstroke pressure-dependent Raman spectra of ZnO at 300 K. The asterisks denote the 202.7 cm^{-1} phonon. (b) Pressure dependence of the observed optical phonons. Solid lines are linear least-square fits to the experimental points.

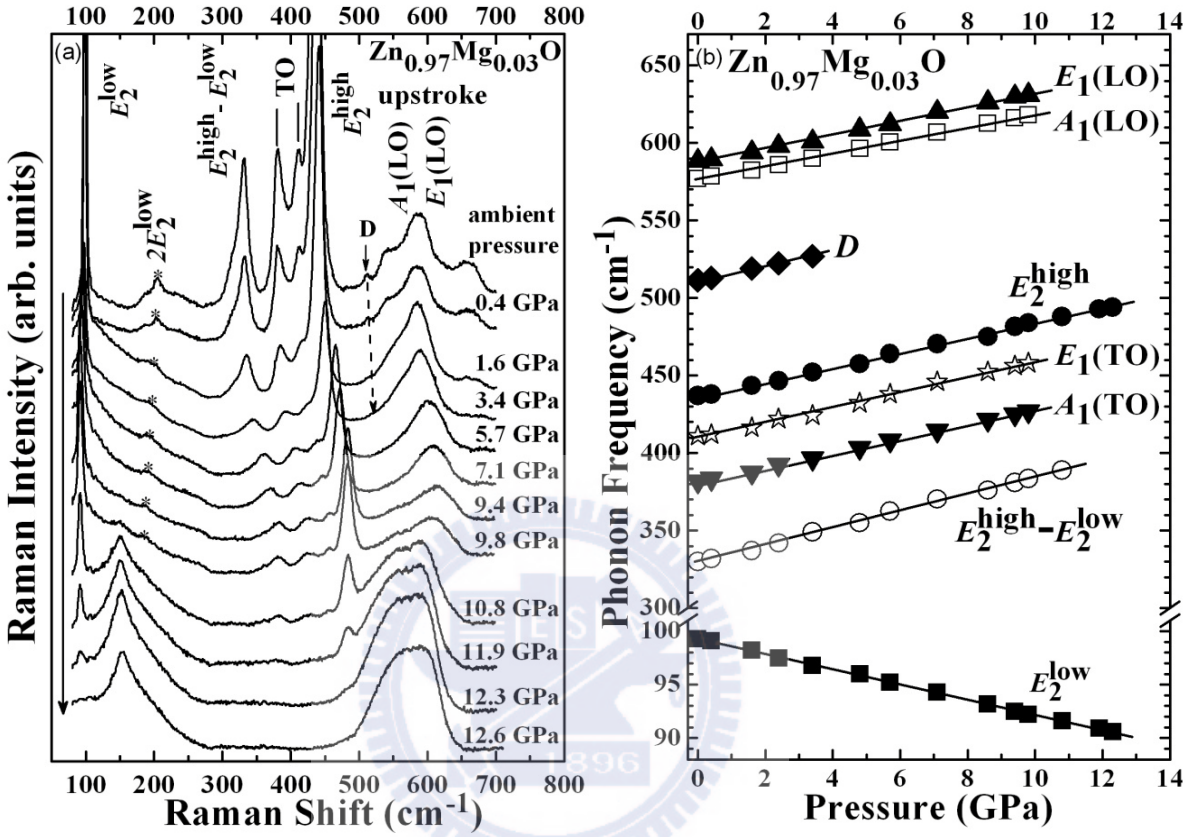

Fig. 3-6. (a) Upstroke pressure-dependent Raman spectra of $Zn_{0.97}Mg_{0.03}O$ at 300 K. The asterisks mark the $2E_2^{low}$ phonon. The behavior of *D* mode is indicated by dashed arrow. (b) Pressure dependence of the observed optical phonons. The solid lines are the linear least-square fits.

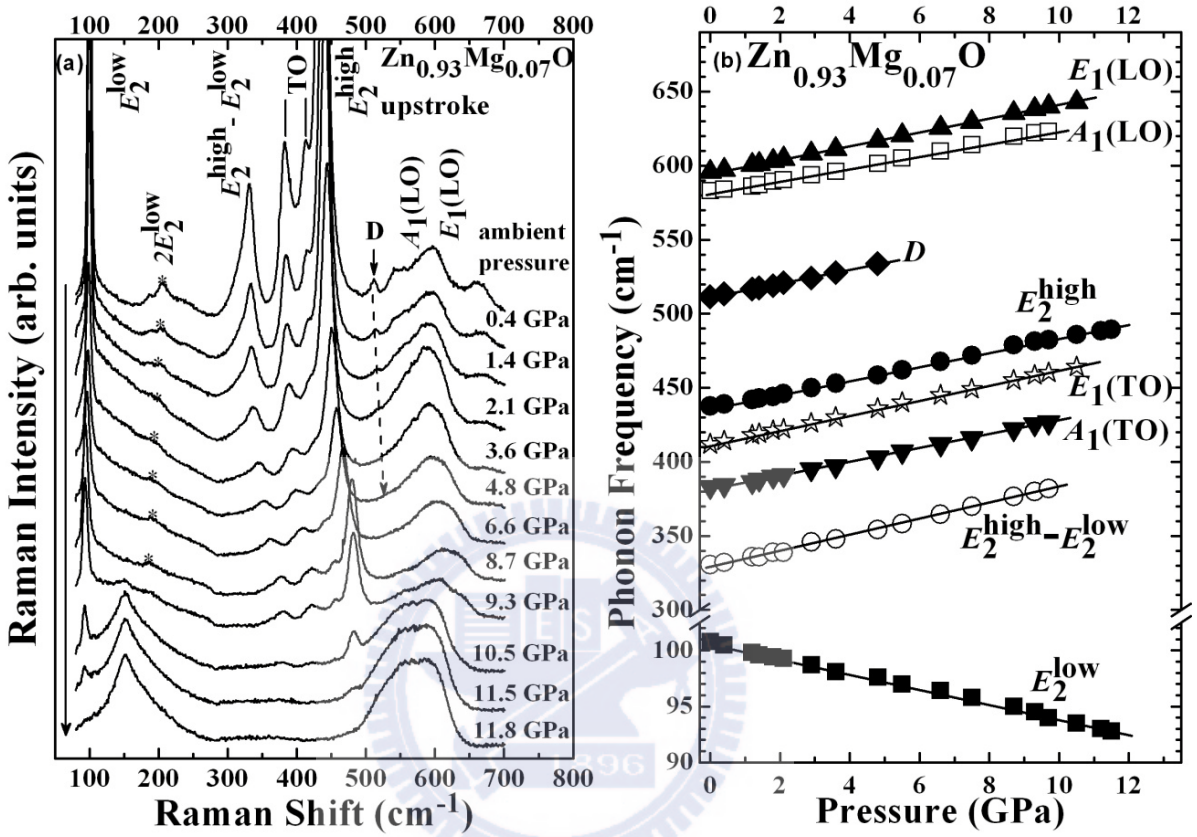

Fig. 3-7. (a) Upstroke pressure-dependent Raman spectra of $Zn_{0.93}Mg_{0.07}O$ at 300 K. The asterisks mark the $2E_2^{low}$ phonon. The behavior of *D* mode is indicated by dashed arrow. (b) Pressure dependence of the observed optical phonons. The solid lines are the linear least-square fits.

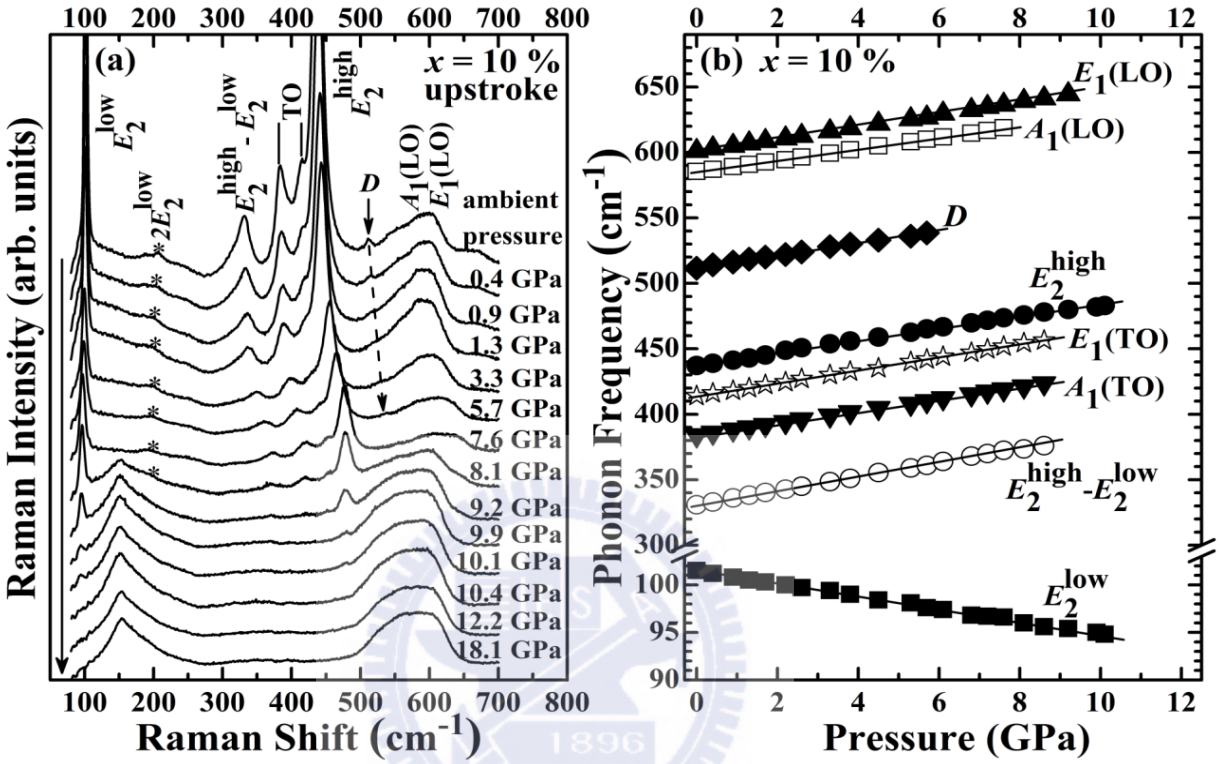

Fig. 3-8. (a) Upstroke pressure-dependent Raman spectra of $Zn_{0.90}Mg_{0.10}O$ at 300 K. The asterisks mark the $2E_2^{low}$ phonon. The behavior of *D* mode is indicated by dashed arrow. (b) Pressure dependence of the observed optical phonons. The solid lines are the linear least-square fits.

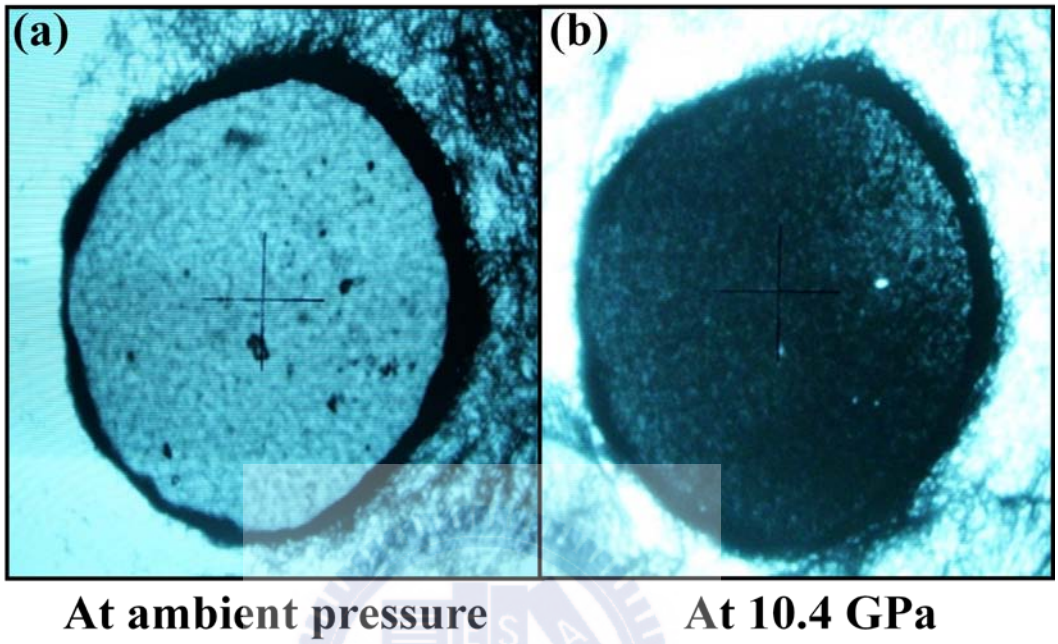

Fig.3-9. The images of the $Zn_{0.90}Mg_{0.10}O$ powders under front illumination in the DAC loaded with ruby chips (a) before the phase transition at ambient pressure and (b) after it is completed at 10.4 GPa.

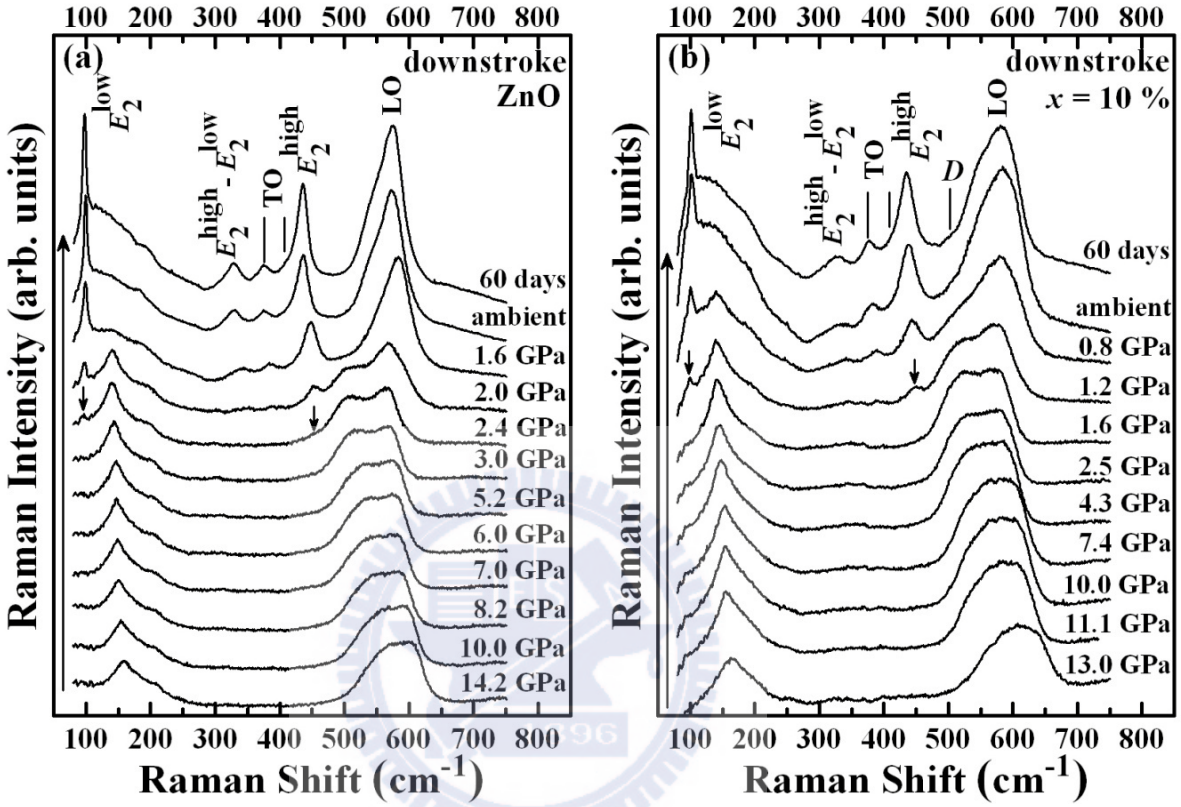

Fig.3-10. Downstroke pressure-dependent Raman spectra of (a) ZnO and (b) $Zn_{0.90}Mg_{0.10}O$ at 300 K. The black arrows indicate the reappearance of the E_2^{low} and E_2^{high} phonons.

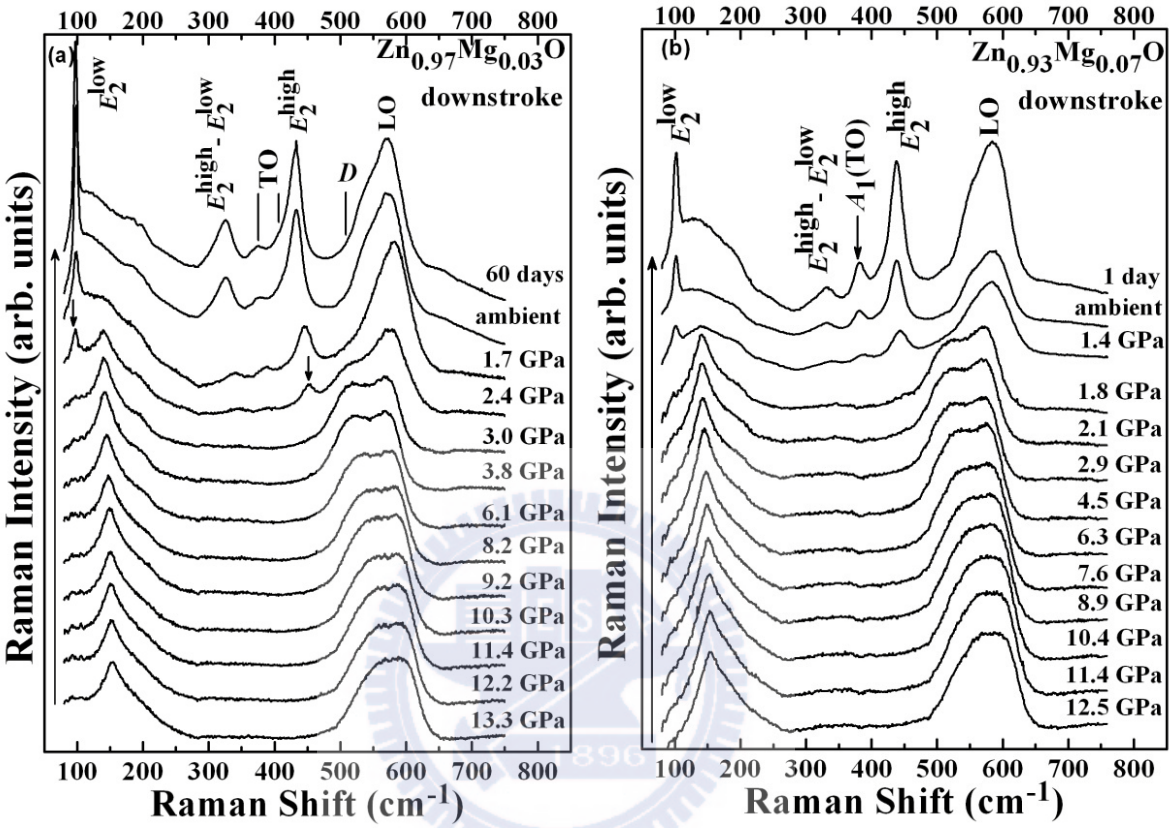

Fig.3-11. Downstroke pressure-dependent Raman spectra of (a) $Zn_{0.97}Mg_{0.03}O$ and (b) $Zn_{0.93}Mg_{0.07}O$ at 300 K. The black arrows indicate the reappearance of the E_2^{low} and E_2^{high} phonons.

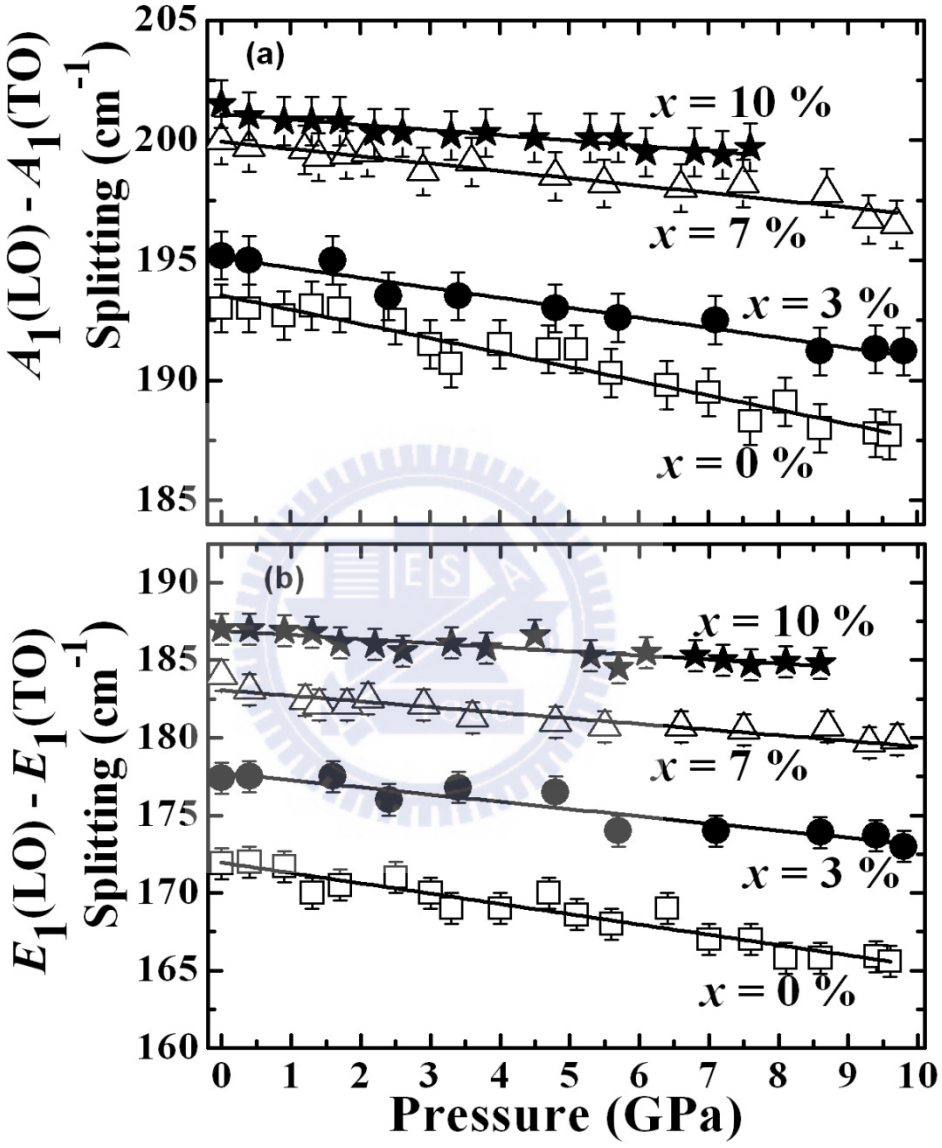

Fig.3-12. Pressure dependence of the LO-TO splitting for both the (a) A_1 and (b) E_1 modes in $Zn_{1-x}Mg_xO$ ($0 \leqq x \leqq 0.10$). Solid lines are the linear least-square fits to the data points.

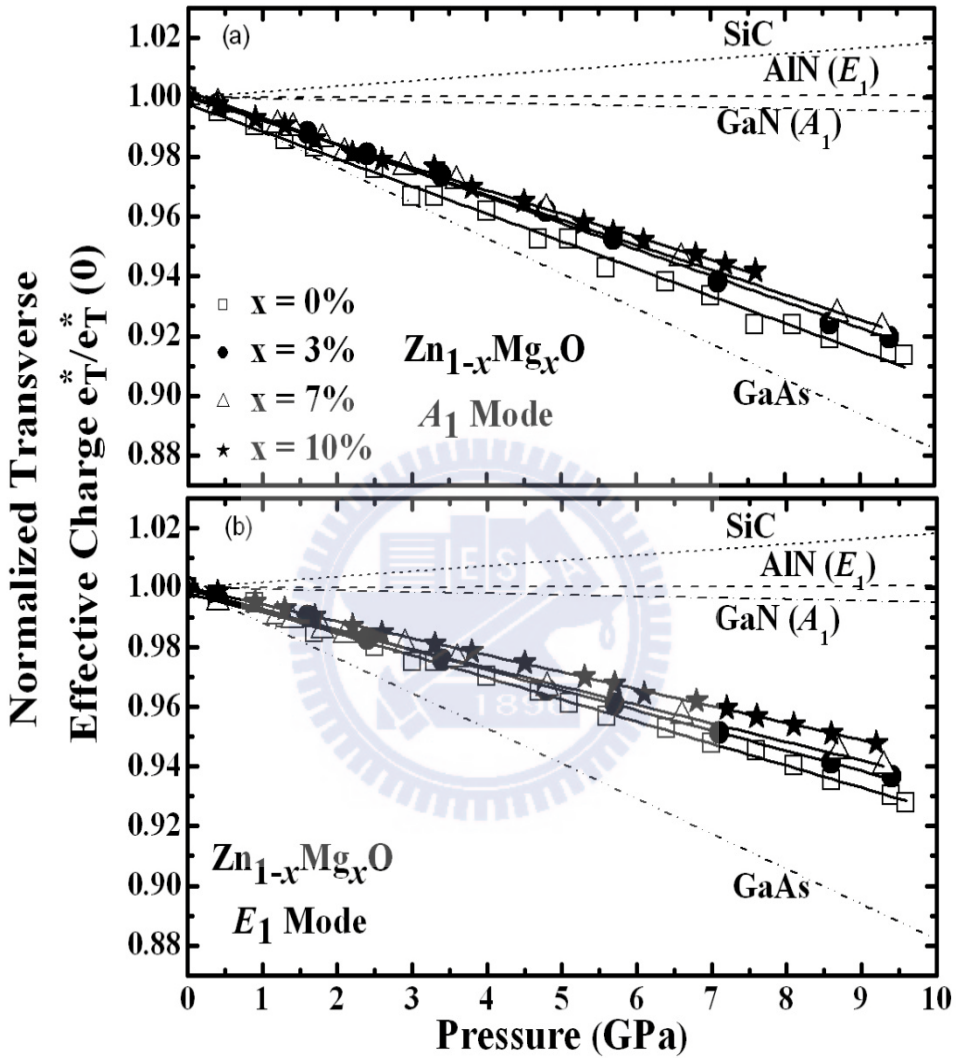

Fig.3-13 The transverse effective charge normalized to its ambient pressure value $e_T^* / e_T^*(0)$ versus the applied pressure for both the (a) A_1 and (b) E_1 modes in $Zn_{1-x}Mg_xO$ ($0 \leqq x \leqq 0.10$). Solid lines are the linear least-square fits. For comparison, the pressure dependence of $e_T^* / e_T^*(0)$ for SiC, AlN, GaN, and GaAs are also plotted.

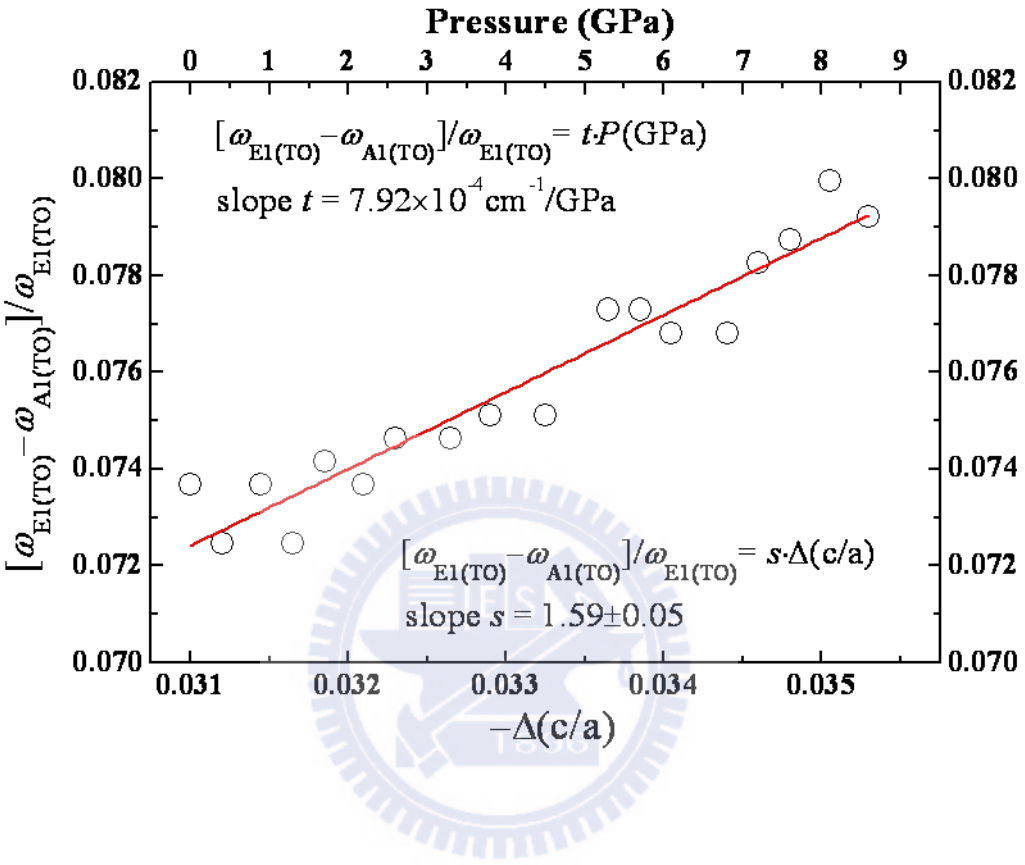

Fig.3-14. Dependence of the $[\omega_{E_1(TO)}-\omega_{A_1(TO)}]/\omega_{E_1(TO)}$ phonon frequency ratio on Δ(c/a) and pressure for $Zn_{0.90}Mg_{0.10}O$.

Chapter 4 Conclusions

This study explored the lattice dynamics and crystalline properties in $Zn_{1-x}Mg_xO$ ($0 \leqq x \leqq 0.10$) using high-pressure Raman spectroscopy. Based on the distinct influences of Mg and external pressure on the lattice dynamic properties of ZnO, the vibrational mode at 202.7, 332.7, and 511.5 cm^{-1} can be assigned as $2E_2^{low}$, $E_2^{high} - E_2^{low}$, and complex Zn_I-O_I phonons, respectively. Detailed pressure-dependent Raman spectra show that the wurtzite-to-rocksalt phase transition of ZnO completes at around 13.2 GPa, which result is consistent with the high-resolution XRD studies. Moreover, the phase transition pressures decrease with increasing Mg concentration. This fact implies that the substituted Mg atoms tend to reduce the crystalline stability of ZnO. Interestingly, we found that the effects of Mg and external pressure on the transverse effective charge of ZnO are opposite. At ambient condition, ZnO becomes more *ionic* upon the incorporation of Mg, while it becomes more *covalent* under high pressure, *i.e.* the LO-TO splitting and the transverse effective charge decrease with increasing pressure. Furthermore, both the incorporated Mg and applied pressure tend to increase the crystal anisotropy of $Zn_{1-x}Mg_xO$. The higher the Mg concentration in the $Zn_{1-x}Mg_xO$, the faster the crystal becomes anisotropy. This result is in accordance with the Mg-induced reduction of the phase transition pressures.

The evolution of strain levels and their distribution in $Zn_{1-x}Mg_xO$ semiconductors relies

on the precise knowledge of phonon deformation potentials which are determined from the obtained phonon pressure coefficients. Moreover, these phonon vibrational parameters are also crucial for further studying the phonon-plasmon interaction to resolve the electron or hole concentration (mobility) in $Zn_{1-x}Mg_xO$ via a nondestructive Raman approach.